Climate Dynamics (1987) 2:63–90

Climate Dynamics

Transport and storage of CO_2 in the ocean — — an inorganic ocean-circulation carbon cycle model

E Maier-Reimer and K Hasselmann

Max-Planck-Institut für Meteorologie, D-2000 Hamburg 13, Federal Republic of Germany

Abstract. Inorganic carbon in the ocean is modelled as a passive tracer advected by a three-dimensional current field computed from a dynamical global ocean circulation model. The carbon exchange between the ocean and atmosphere is determined directly from the (temperature-dependent) chemical interaction rates in the mixed layer, using a standard CO_2 flux relation at the air-sea interface. The carbon cycle is closed by coupling the ocean to a one-layer, horizontally diffusive atmosphere. Biological sources and sinks are not included. In this form the ocean carbon model contains essentially no free tuning parameters. The model may be regarded as a reference for interpreting numerical experiments with extended versions of the model including biological processes in the ocean (Bacastow R and Maier-Reimer E in prep.) and on land (Esser G et al. in prep.). Qualitatively, the model reproduces the principal features of the observed CO_2 distribution in the surface ocean. However, the amplitudes of surface pCO_2 are underestimated in upwelling regions by a factor of the order of 1.5 due to the missing biological pump. The model without biota may, nevertheless, be applied to compute the storage capacity of the ocean to first order for anthropogenic CO_2 emissions. In the linear regime, the response of the model may be represented by an impulse response function which can be approximated by a superposition of exponentials with different amplitudes and time constants. This provides a simple reference for comparison with box models. The largest-amplitude (~ 0.35) exponential has a time constant of 300 years. The effective storage capacity of the oceans is strongly dependent on the time history of the anthropogenic input, as found also in earlier box model studies.

Introduction

The storage and transport of carbon in the climate system has received increasing attention in past years, both with respect to the problem of projecting the currently observed increase of atmospheric CO_2 levels into the future and, more recently, with regard to past CO_2 fluctuations and their relation to natural climate variability. A central issue in these studies has been the uptake of CO_2 by the ocean (Revelle and Suess 1957; Keeling 1973; Bolin 1975; Bolin et al. 1979; Bacastow and Björkström 1981; National Academy Report 1982; Edmonds et al. 1984; Sundquist and Broecker 1985). Since the beginning of well-calibrated recordings in 1958, the CO_2 content of the atmosphere has increased by 9% from 315 ppm to 344 ppm (Keeling et al. 1982). Estimates of the net anthropogenic release of CO_2 through fossil-fuel burning, cement production and land use would yield approximately twice this increase if all emissions remained in the atmosphere (Rotty 1983). It is therefore generally concluded that the oceans must have absorbed approximately half of the anthropogenic CO_2 input. However, this estimate is uncertain because of the unknown uptake or release of CO_2 by the terrestial biosphere. Attempts to compute the partitioning of the anthropogenic CO_2 input between the three main reservoirs, atmosphere—ocean—terrestial biosphere, using carbon cycle models have suffered from basic model limitations. In addition to difficulties in assessing the role of the terrestrial biosphere, the strongly simplified representation of the ocean uptake in the form of box models has represented a major source of uncertainty. The lack of a quantitative ocean carbon cycle model has similarly handicapped discussions on the causes of past CO_2 fluctuations (cf. Berger and Keir 1984).

Current box models of the ocean carbon cycle attempt to simulate the transport and storage of carbon by the complex current system of the real global ocean circulation in terms of rather simple exchange systems consisting of relatively few reservoirs (typically between 2 and 20). Although box models can be calibrated to reproduce average tracer distributions (tritium, natural and bomb-made ^{14}C) satisfactorily, the necessarily rather arbitrary projection of the true system onto such strongly simplified approximations yields significant differences in the response characteristics of different models (cf. Keeling 1973; Oeschger et al. 1975; Siegenthaler and Oeschger 1978; Björkström 1979; Killough and Emanuel 1981; Viecelli et al. 1981; Sundquist 1985). These difficulties can clearly be removed only by developing ocean carbon cycle models based on a realistic description of the three-dimensional global ocean circulation derived from high-resolution dynamical models. In contrast to box models, such models contain essentially no tunable parameters. The CO_2 transport and storage properties of the ocean are completely determined by the prescribed ocean dynamics and chemistry; and the tracer distributions serve only to test the model, not to calibrate it.

The development of more realistic ocean CO_2 storage models is particularly important if the models are to be applied to projections of future atmospheric CO_2 levels for different CO_2 emission scenarios. Different regions of the ocean affect the CO_2 storage on different time scales: on the seasonal time scale, only the mixed layer and seasonal thermocline are effective; for intermediate time scales of 10—20 years, the warm water sphere extending through the main thermocline is the main reservoir; while for longer time periods, up to several hundred years, the principal uptake is by the deep ocean. On the basis of this multi-time-scale structure, it has been pointed out (e.g. Oeschger et al. 1975) that a significant reduction of the CO_2 emission growth rate (which was characterized prior to 1980 by an *e*-folding time scale of the order of 30 years) could strongly increase the effective storage capacity of the oceans by enabling a stronger coupling into the deep ocean. Thus, a reduction of CO_2 emissions would result in an over-proportional reduction in the projected atmospheric CO_2 concentration. A quantitative calculation of these time dependence effects with the aid of a realistic ocean CO_2 storage model is clearly an essential prerequisite for reliable projections of future atmospheric CO_2 levels for different emission scenarios.

Another important application of a dynamical ocean carbon cycle model is the evaluation of climatic feedback effects. Recent computations of the response of the ocean circulation to a projected future change in the atmospheric circulation resulting from a CO_2 increase (Bryan and Spelman 1986) indicate that the reduction of the oceanic heat loss at higher latitudes due to atmospheric warming leads to a reduced deep-ocean overturning. This would reduce the rate of CO_2 uptake by the ocean by reducing the CO_2 transport into the deep ocean. The net result is a positive feedback of the climatic response to CO_2 emissions (see also Broecker and Takahashi 1984). This can clearly be computed quantitatively only with an ocean carbon model based on the 3d ocean circulation.

Climate feedback effects are also essential for theories of natural climate variability involving CO_2 changes. The discovery of significant variations in the past CO_2 content of the atmosphere in ice cores (Neftel et al. 1982; Berner et al. 1979; Delmas et al. 1980) has stimulated a number of speculations on climate variability associated with variations in the relative CO_2 content of the atmosphere and ocean. Generally, these involve some form of interaction between the ocean circulation and the uptake of CO_2 by the biota in the oceans. Again, these concepts can be explored quantitatively only with realistic coupled ocean circulation and carbon cycle models.

In this paper we describe the inorganic version of a high-resolution ocean carbon cycle model. An earlier version of the model, based on an earlier ocean circulation model with lower vertical resolution, was outlined in Maier-Reimer (1984). The ocean circulation is treated as a frozen 3d velocity field, derived from the asymptotic steady state of a wind and thermodynamically driven ocean circulation model. The carbon constituents are advected by this current field as conservative tracers, interacting chemically only in the uppermost mixed layer where the ocean exchanges CO_2 with the atmosphere in accordance with a standard bulk flux relation. Vertical mixing is introduced only at grid points (mainly at high latitudes) for which vertical mixing occurred also in the dynamical model. The chemical interactions in the mixed layer are computed using a seven-component inorganic system. Thus, the buffer factor is derived explicitly from the interaction relations.

To close the system, the ocean carbon model is coupled to a one-layer, meridionally diffusive atmosphere. In the zonal direction the atmosphere

is assumed to be fully mixed. For most of the applications considered here, involving time scales large compared with 1 year, the atmosphere could in fact have been treated still more simply as a single homogeneously mixed box.

Sources or sinks of carbon associated with the oceanic biota or the terrestrial biosphere are not considered. Extensions of the model to include these effects are presented in Bacastow R and Maier-Reimer E (in prep.) (referred to in the following as BMR) for ocean biota and Esser G et al. (in prep.) for the terrestrial biosphere. The present version of the model also contains no source term for river input and no sink due to sedimentation. A specific investigation of the basic inorganic ocean carbon cycle model without these extensions is nevertheless useful for three reasons:

i) For an understanding of the ocean carbon cycle it is important to distinguish between those properties of the chemical distributions which are determined by the large-scale ocean overturning, together with regional differences in the (temperature-dependent) surface solubilities, and those properties which are governed by the 'biological pump', in which dissolved inorganic carbon is converted in the upper ocean into particulate organic matter which rains down and is returned to the dissolved inorganic carbon pool in deeper layers.

ii) The restriction to the inorganic cycle facilitates the comparison with idealized box models, which similarly exclude biological sources and sinks in their simplest form.

iii) For the storage of anthropogenic CO_2 emissions in the ocean, an inorganic ocean carbon cycle serves as a valid first approximation since ocean water has a sufficiently high carbon concentration that any additional CO_2 uptake has very little impact on the oceanic biological cycle. The biological cycle affects the anthropogenic CO_2 response only indirectly and nonlinearly by modifying slightly the reference state on which the anthropogenic sources act. This argument does not apply to the terrestrial biosphere, but here it is again useful to study first the influence of the ocean in isolation before turning to the complete system.

The ocean circulation model used to produce the advection field for the ocean carbon cycle model is outlined briefly in the next section. A more detailed description is given in Maier-Reimer E et al. (1982, 1987 in prep.). The carbon cycle model is described in the subsequent section. The model is then applied to simulate the pre-industrial distributions of ^{12}C and ^{14}C in the ocean. These are compared with the distributions computed with the ocean cycle model including biospheric fluxes by Bacastow R and Maier-Reimer E (in prep.). The CO_2 response of the coupled ocean-atmosphere system to past anthropogenic CO_2 emissions is then computed. An interpretation of these results in terms of the impulse response (Green) function of the system, computed from a step-function increase in CO_2, is given. Projections of future atmospheric CO_2 concentrations for different CO_2 emission scenarios are presented and the conclusions are summarized. The Appendix provides further details on the computation of the chemical interactions within the seven-component mixed-layer system which determine the effective buffer factor.

The ocean circulation model

The current field used to advect the chemical constituents of the carbon cycle was computed with a global ocean circulation model (Maier-Reimer et al. 1982; Maier-Reimer et al. 1986), based on a proposal by Hasselmann (1982). Gravity waves, which give rise to the rather short time-step requirements for conventional primitive-equation circulation models (e.g. Bryan 1969), are filtered out by applying appropriate quasi-geostrophic approximations. The circulation is divided into a barotropic component, consisting of the vertically averaged current and surface displacement fields, and a baroclinic component, consisting of the residual current after subtraction of the barotropic contribution, and the temperature and salinity fields. On the time scales of interest, the velocity fields are in geostrophic balance and the more rapidly responding barotropic mode equilibrates quasi-instantaneously with the forcing surface stress and density fields, leaving only the salinity and temperature fields of the baroclinic component as prognostic variables. The model is closed by frictional layers at the equator and at the coasts. Additional terms are introduced near the equator to correct for the breakdown of geostrophy in this region. Details are given in Maier-Reimer et al. (1982) and Maier-Reimer E et al. (in prep.).

Except for some unavoidable numerical diffusion and mixing arising from convective overturning at high latitudes, salinity and temperature are transported in the model by advection only. This

is an important distinction from most ocean box models, in which vertical transports into the deep ocean are generally assumed to be governed by both vertical diffusion and vertical advection. Since the storage response curves for diffusive and advective models have different time dependence, there is no guarantee that a simple diffusive box model can be tuned to agree with an advective circulation model on all time scales.

For the present application, the model was run on a $5° \times 5°$ global grid with ten vertical levels. Horizontal velocity, temperature and salinity were specified at depth levels 75, 150, 250, 450, 700, 1000, 2000, 3000, 4000 and 5000 m, while vertical velocity was defined at the intermediate levels 112, 200, 350, 575, 850, 1500, 2500, 3500 and 4500 m. The model included a realistic bottom topography. The circulation was driven by the observed wind stress field, taken from Hellerman (1967), and observed surface values of salinity and temperature, from Levitus and Oort (1977). The model was spun up from a homogeneous initial state and run for 3000 years to an equilibrium state. A seasonal cycle was included, but for the present study we use only the annually averaged velocity fields. The seasonality is nevertheless important, as it strongly influences the regions and frequency of overturning. These determine the degree of mixing between the surface layer and the deeper layers at high latitudes, which is then introduced with the same strength into the carbon model. Figure 1 shows the regional distribution of convective events. They are most abundant in the Antarctic belt. Although the global formation of deep water appears to be well simulated by the model, the model resolution is inadequate to reproduce all regional features satisfactorily. In particular, the transport of Arctic deep water through the narrow channels across the Iceland-Faroe ridge cannot be properly resolved. Another factor leading to the underestimation of deep-water formation in this region in the present model is the suppression of brine expulsion through freezing due to the prescription of the sea surface temperature as a boundary condition. Improved deep-water formation rates in the North Atlantic were achieved with models including a prognostic sea ice description (Princeton-Hamburg North Atlantic model intercomparison study, Willebrand et al. pers. comm.).

Figures 2 and 3 show the horizontal velocity field in the uppermost layer (75 m) and the associated vertical velocity field below the layer (112 m). The horizontal velocities represent a superposition of the Ekman drift and the geostrophic current. The principal ocean surface current systems are seen to be reproduced quite well. The vertical velocity at 112 m is proportional to the divergence of the net current, which at this level is dominated by the Ekman term.

The structure of the water mass transport in deeper levels is best represented in terms of the flow field on surfaces of constant density. As potential density is conserved below the mixed layer, for purely advective transport all water parcel trajectories lie within these surfaces. Figures 4 and 5 show the depths of the isopycnal surfaces $\sigma_T = 26.5$ and $\sigma_T = 27.5$. The surface $\sigma_T = 26.5$ characterizes the main thermocline gyres and the equatorial undercurrent, while the isopycnal

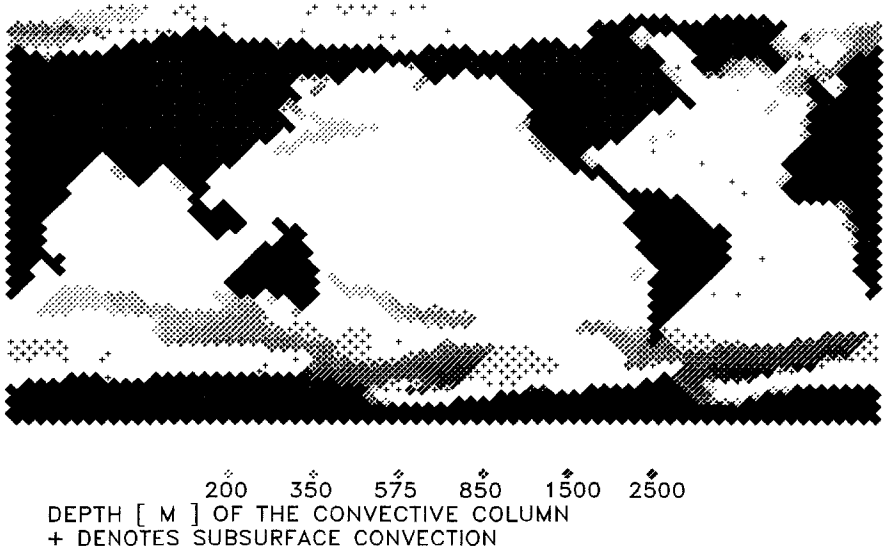

Fig. 1. Depth of the convective column (in m) interacting with the surface. Regions of subsurface convection are marked by '+'

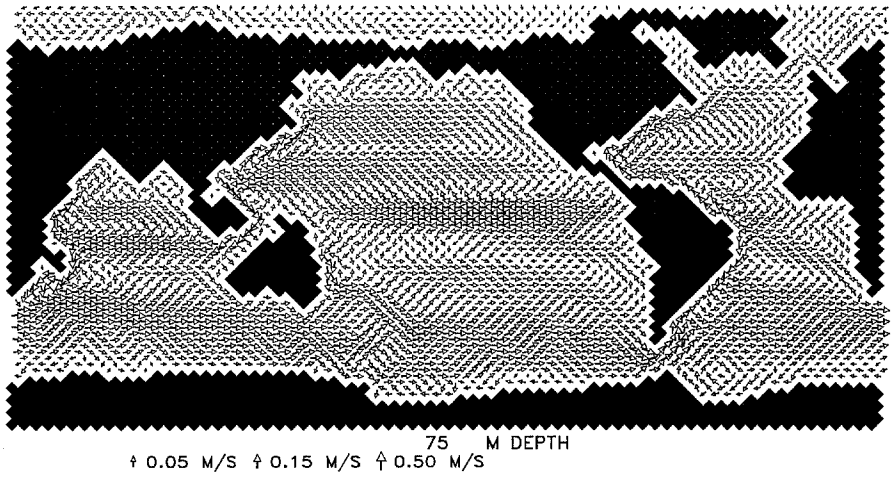

Fig. 2. Horizontal velocity field in the surface layer (75 m depth). Current velocities are proportional to the size of *arrows*

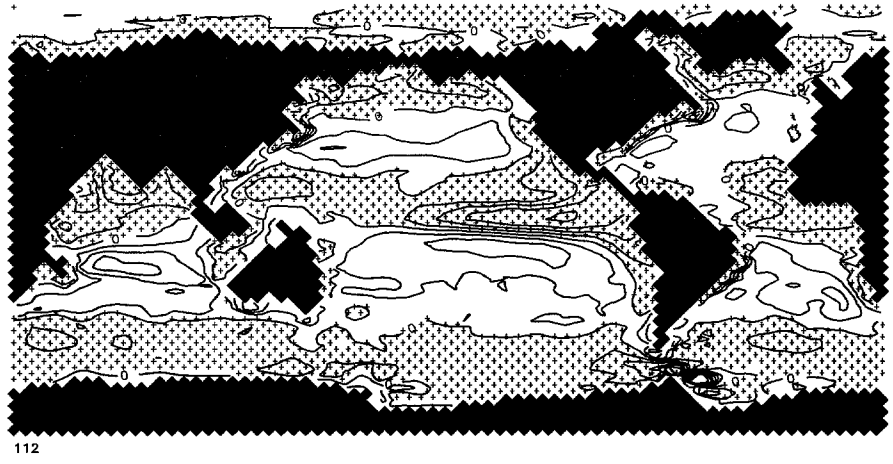

Fig. 3. Vertical velocity field below the surface layer (112 m depth). Regions of positive upward velocities are marked '+'. Contour interval: 10^{-6} m/s. The principal contribution is Ekman suction and pumping

Fig. 4. Depth contours and horizontal velocity field of $\sigma_T = 26.5$ isopycnal surface. Depth contour interval: 100 m

$\sigma_T = 27.5$ lies in the deeper ocean (see also Figs. 8c and 9c). The equatorial upwelling region and the depression of the isopycnals in the main gyres stand out clearly. The flow approximately follows the constant depth contours in most regions of the ocean, but areas of upwelling and downwelling occur where the flow crosses contours. Near the outcropping boundaries, however, variations in the isopycnal depth are generally the result of water mixing rather than rising or sinking motion.

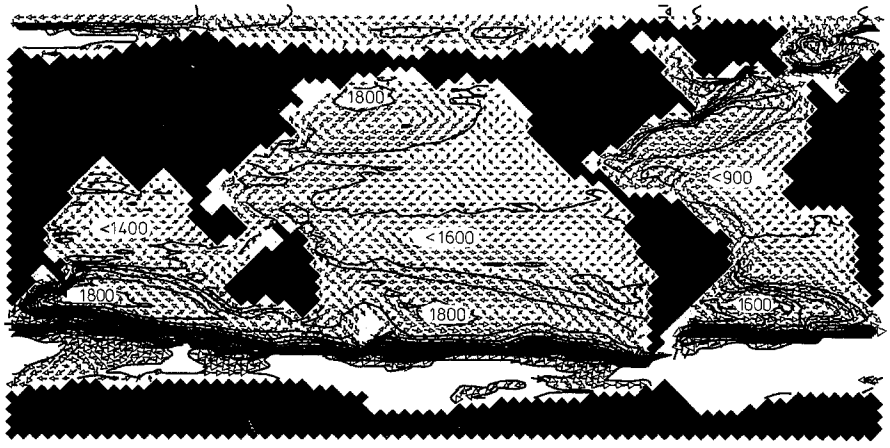

Fig. 5. Depth contours and velocity field of $\sigma_T = 27.5$ isopycnal surface. Depth contour interval: 100 m

The meridional overturning structure of the global ocean circulation is illustrated by the stream function for the zonally averaged current field in Fig. 6. Since the zonal average is taken over all three oceans no significance can be attached to details, but the basic cellular meridional structure with upwelling along the equator and the Antarctic Circumpolar Current and downwelling in the intermediate mid-latitude regions is clearly seen. These features impress a strong signature also on the surface pCO_2 distribution. The effective ventilation of the deep ocean is in fact significantly stronger than implied by the zonally averaged transports shown in the figure, since circulation patterns in the longitude-depth planes are filtered out by the averaging.

Another important factor controlling the surface pCO_2 field is the sea surface temperature (SST) distribution, shown in Fig. 7. Through the formulation of the surface temperature boundary condition, the SST values automatically lie rather close to the prescribed surface air temperatures

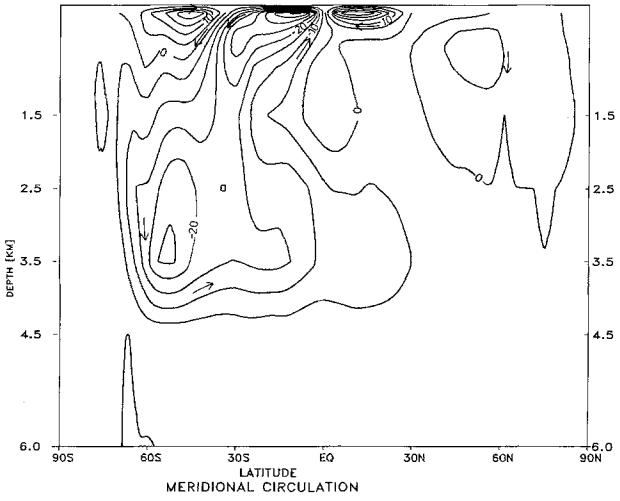

Fig. 6. Meridional stream function for zonally integrated v, w velocity field. Contour interval: 5×10^6 m^3/s

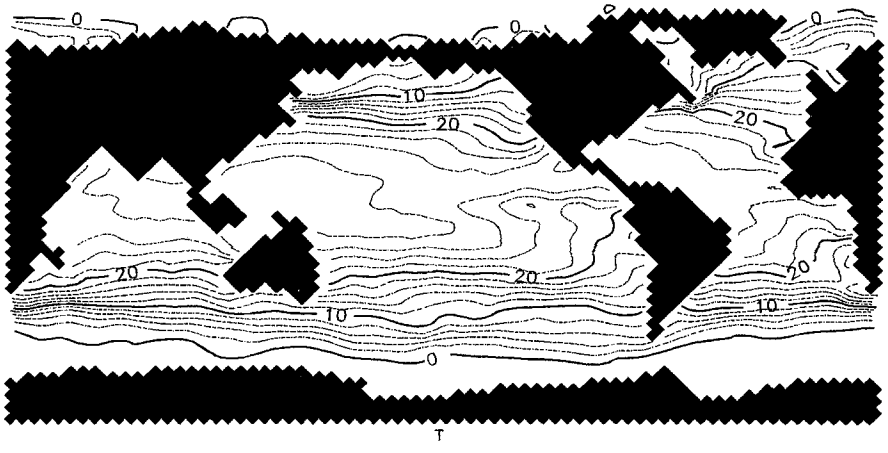

Fig. 7. Model sea surface temperatures (in °C)

and do not represent a critical test of the circulation model. However, Fig. 7 provides a useful reference for interpreting the surface pCO_2 fields computed later with the carbon model.

Figures 8 and 9 show a comparison of the computed and observed T, S sections for the GEOSECS NS section through the Western Pacific. Also shown in Fig. 8c are the computed σ_T sections for reference with Figs. 4 and 5. A similar level of agreement is also found for the other basins. A satisfactory representation of the T, S distribution, both in the main thermocline and the deep ocean, is clearly an important requirement for the validity of the model for water mass transport applications.

An independent test of the transport properties of the model on the 10- to 20-year time-scale characteristic of the main thermocline is given by a comparison of the modelled and observed distributions of tritium from bomb tests, which had a peak input in 1963—1964. Figure 10 shows the computed tritium distribution for an Atlantic GEOSECS section for 1973. As input function, we took the values computed by Weiss and Roether (1980) for the years 1950—1973. These were based on the zonally averaged precipitation for each of the three major oceans, estimated with a zonal resolution of 5°, and included an additional (significant) source from river runoff at the eastern and western boundaries.

The development of a lower-layer tritium tongue indicates that the model is able to capture not only the transport in the main thermocline, but also the mechanism of deep-water formation by convection in high latitudes, although the deep-water formation for the North Atlantic is underestimated (see discussion above).

A test of the residence times in the 100- to 500-year time-scale range characteristic of the deep ocean is provided by the ^{14}C distributions, Figs. 11 and 12. The theoretical distributions were computed using the inorganic carbon cycle model (cf. next section), assuming the same air-sea flux relations for ^{14}C as for ^{12}C. Again, a reasonable agreement between model and observations is found. In particular, the model is seen to reproduce the older waters in the deep North Pacific and the younger waters of the Atlantic quite well.

The use of ^{14}C as a passive tracer to test the circulation model is in fact not quite consistent since, in contrast to the other scalar fields shown in Figs. 7—10, ^{14}C is not simply advected by the current field but is also transported vertically through the biological pump. The downward flux

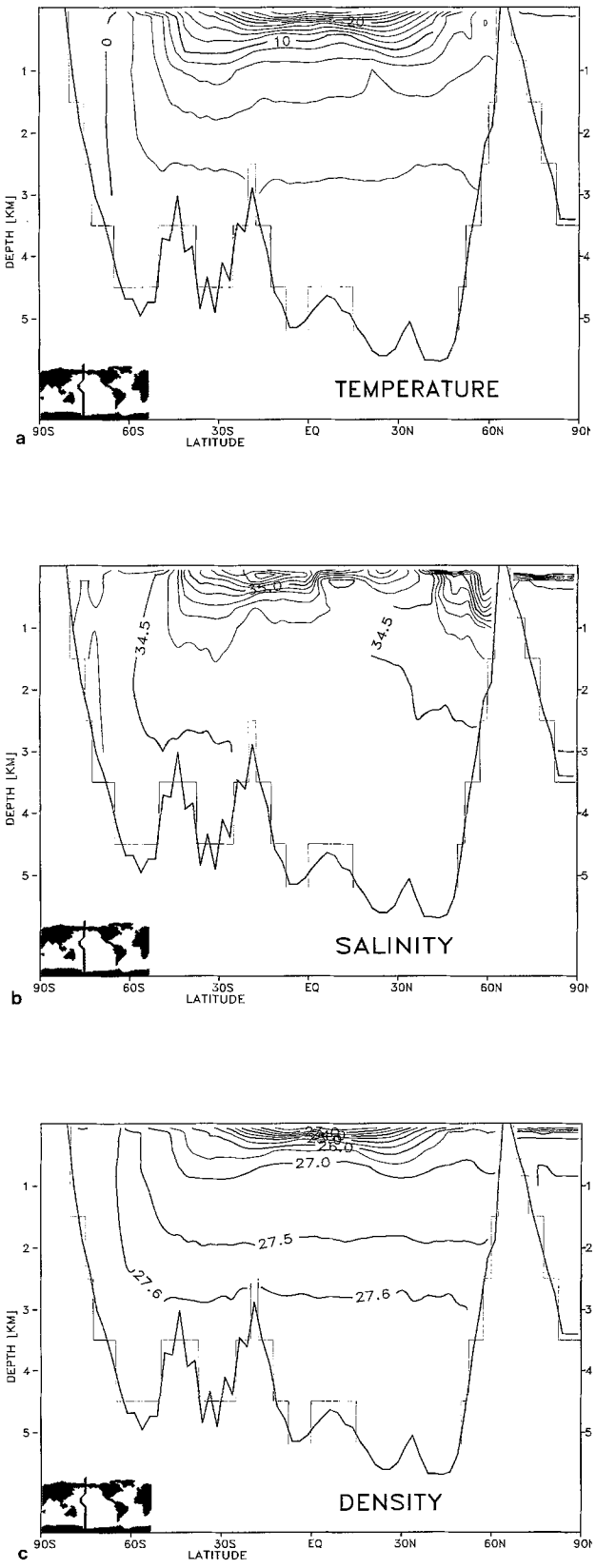

Fig. 8a—c. Sections of **a** potential temperature (°C), **b** salinity (‰) and **c** potential density σ_T, computed by the circulation model for the Western Pacific section indicated in the inset

WESTERN PACIFIC

POTENTIAL TEMPERATURE [°C]
SEP. 1973 - MAR. 1974

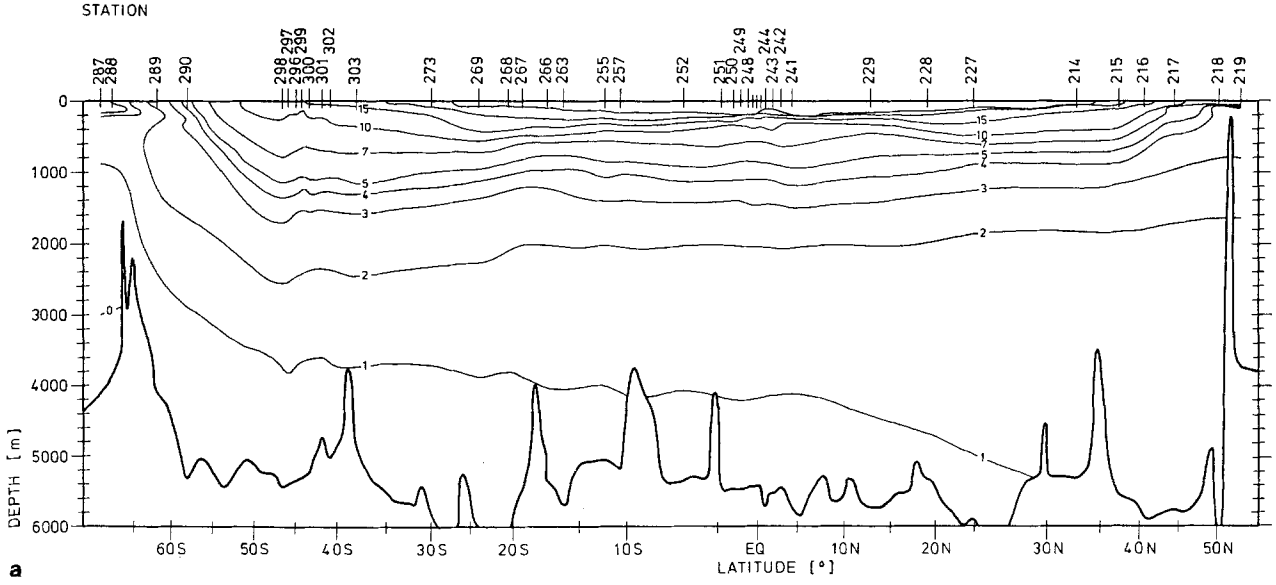

a

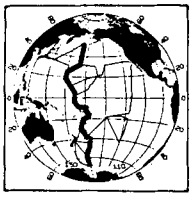

WESTERN PACIFIC

SALINITY [‰]
SEP. 1973 - MAR. 1974

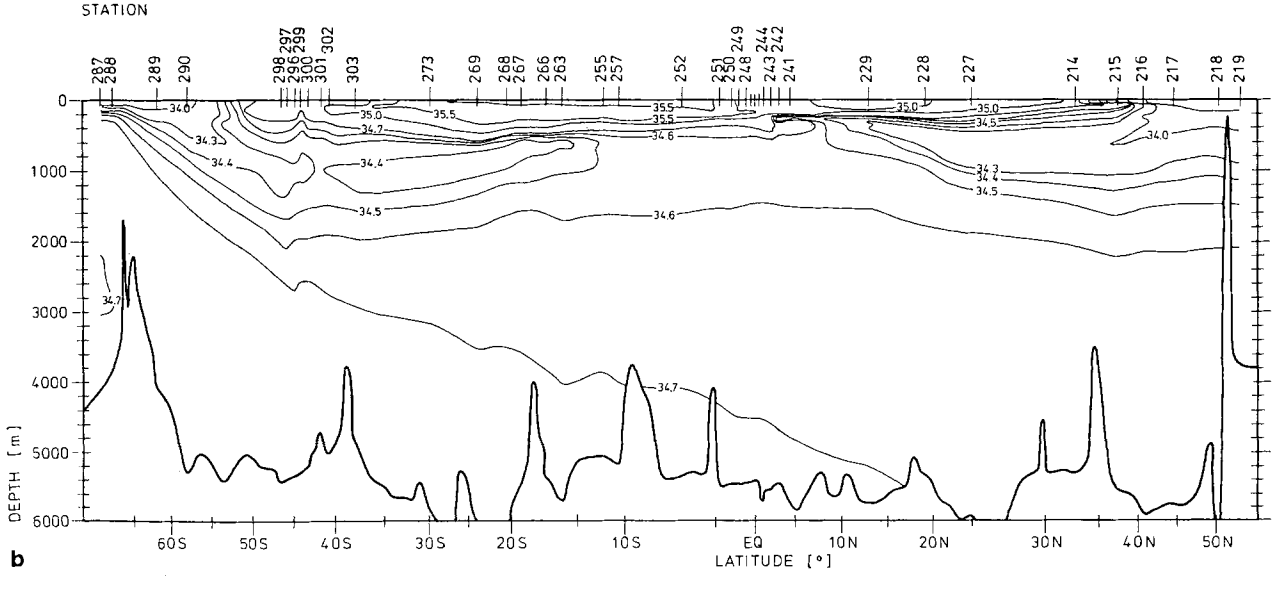

b

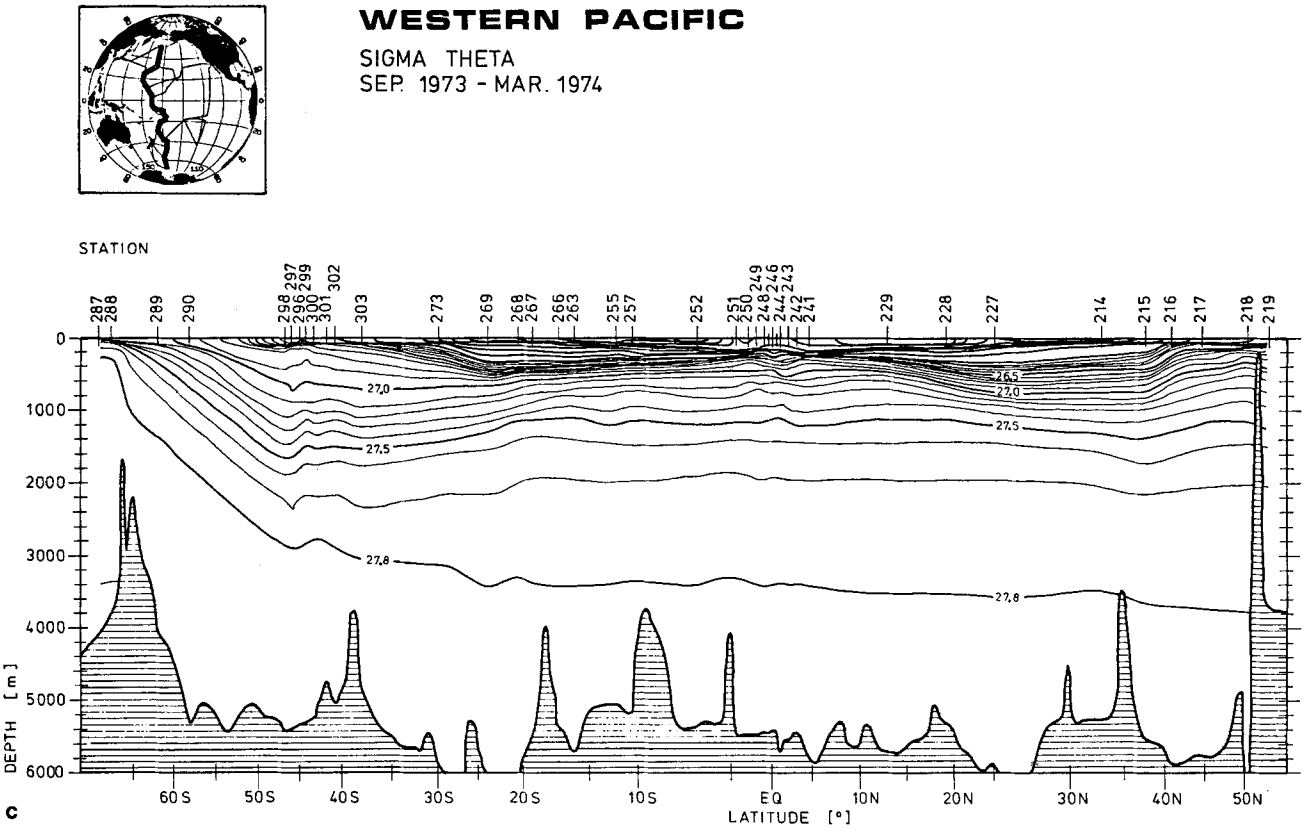

Fig. 9a—c. Measured sections of **a** potential temperature (°C), **b** salinity (‰) and **c** σ_T, for the GEOSECS Western Pacific section (from Craig et al. 1981)

of ^{14}C from the biologically active surface layers in the form of falling particulate matter results in increased residence times of ^{14}C in the deeper ocean layers in which the particles are remineralised. Figure 13 shows the corresponding ^{14}C section for the Western Pacific computed with the same ocean circulation model, but including the effects of the biota in the ocean carbon cycle model (from BMR). The agreement with observations is seen to improve slightly if this effect is included. (The fact that biota are not included in the version of the carbon cycle model used in the present paper does not, of course, remove the need to allow for this effect when assessing the residence times predicted by the ocean circulation model.)

The increase in the apparent age of the deep water through the biological activity appears rather surprising at first sight. However, it should be noted that the carbon pump is effective mainly in regions of high productivity, which are associated with upwelling. Thus, the pump returns ^{14}C from surface waters which are already depleted in ^{14}C (rather than from 'young' surface water) to deeper layers, thereby increasing the net residence time of ^{14}C in the deep ocean.

The above discussion of ^{14}C in the ocean applies only to the stationary, natural, pre-industrial ^{14}C distribution. We shall consider the question of changes of the ^{14}C distribution in the ocean in a later section together with the changes which have occurred in the ^{12}C distribution during the last 150 years. This requires taking into account the dilution of ^{14}C through the release of ^{14}C-depleted CO_2 from fossil fuel (Suess effect) and the increase of ^{14}C through the input of ^{14}C from bomb tests.

A more detailed analysis of the model dynamics and water mass transport and transformation properties is given in Maier-Reimer E et al. (1982, 1987 in prep.). The fields are not fundamentally different from previous computations, e.g., by Bryan and Lewis (1979) and other workers (cf. also Bryan 1979). However, the thermocline appears somewhat shallower in the present model, in closer agreement with observations. Presumably this is because no explicit diffusion is introduced into the present model.

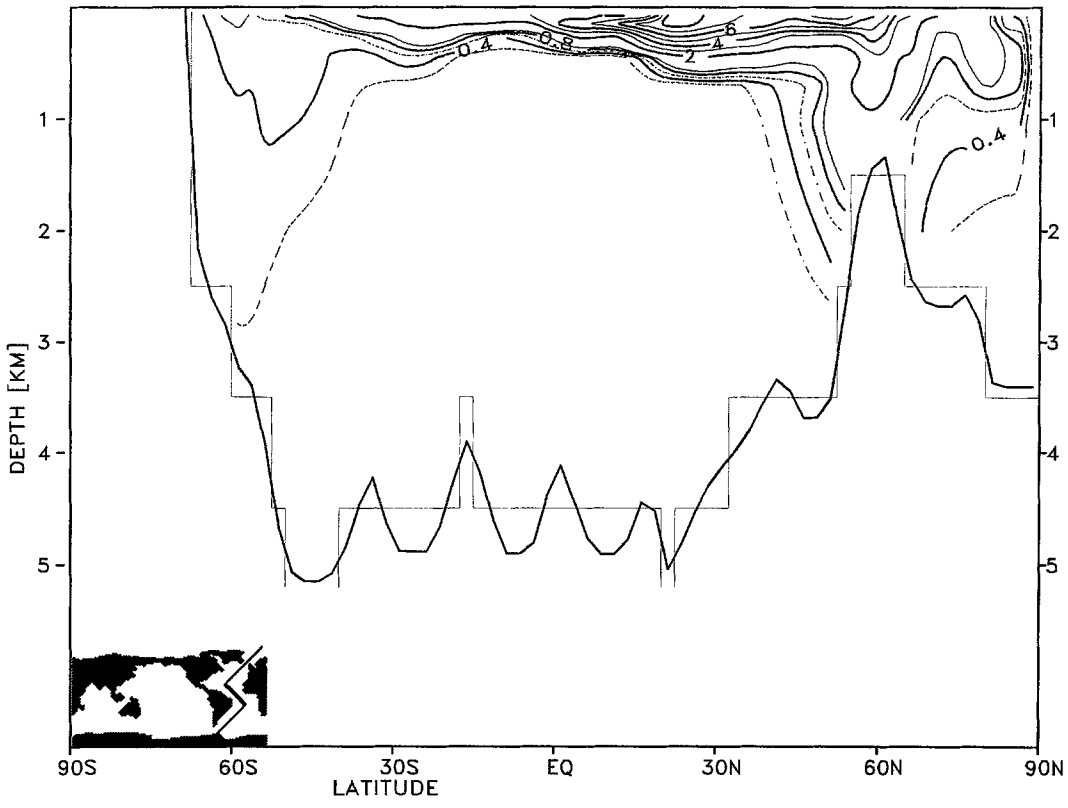

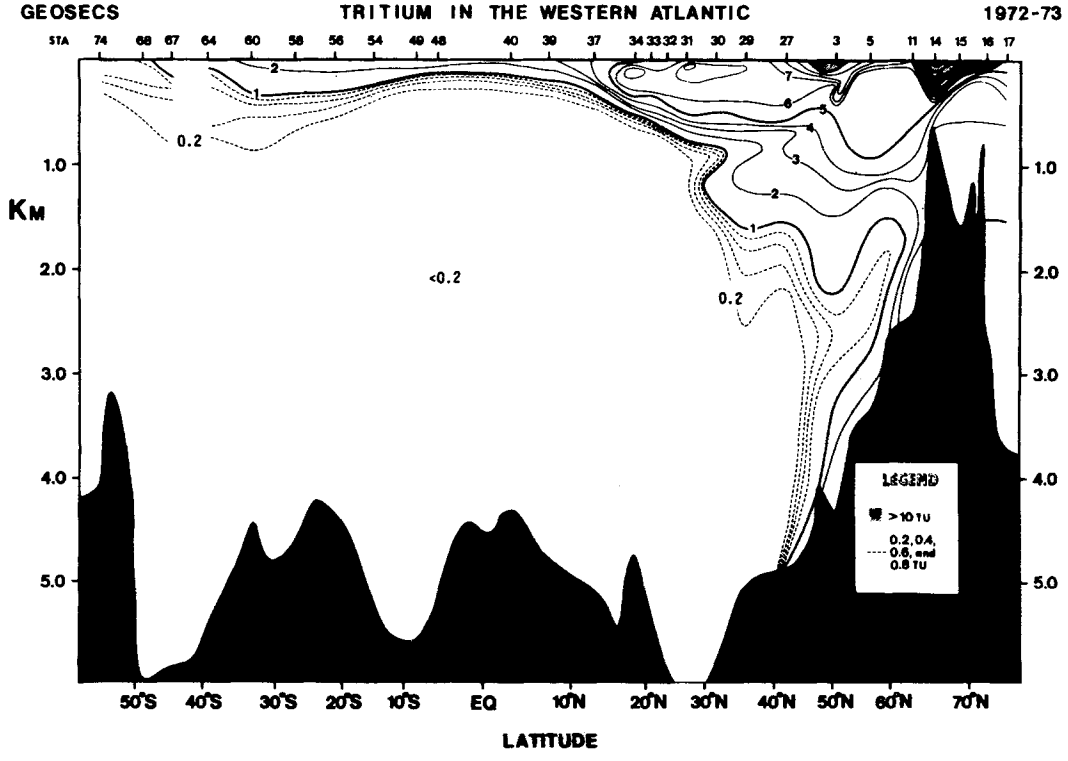

Fig. 10a and b. Tritium Atlantic sections according to **a** model and **b** GEOSECS observations from Östlund et al. 1976)

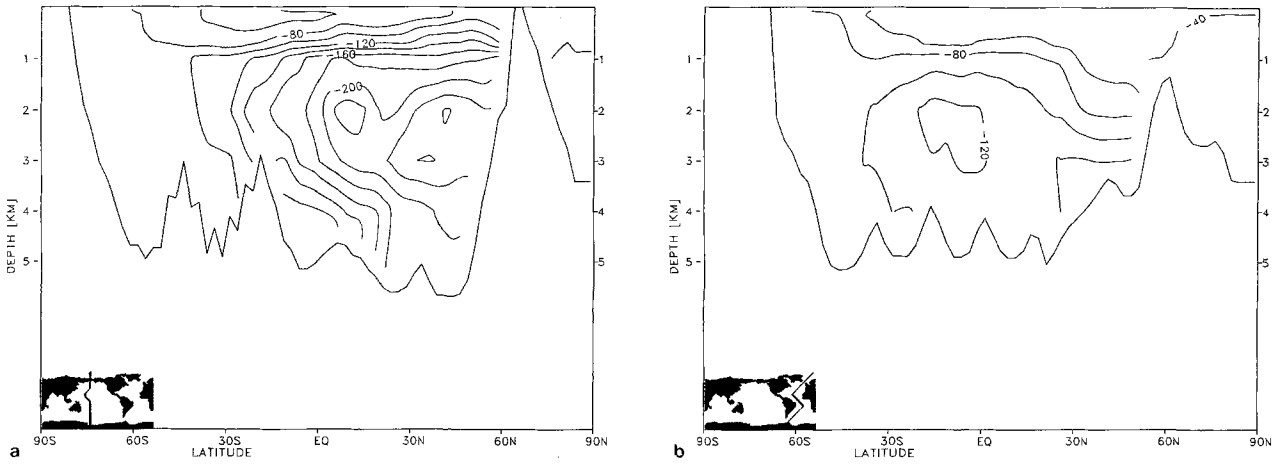

Fig. 11a and b. Model $\Delta^{14}C$ distributions for **a** the Western Pacific and **b** Atlantic sections. The distributions were computed with the advective tracer model without inclusion of the biological pump

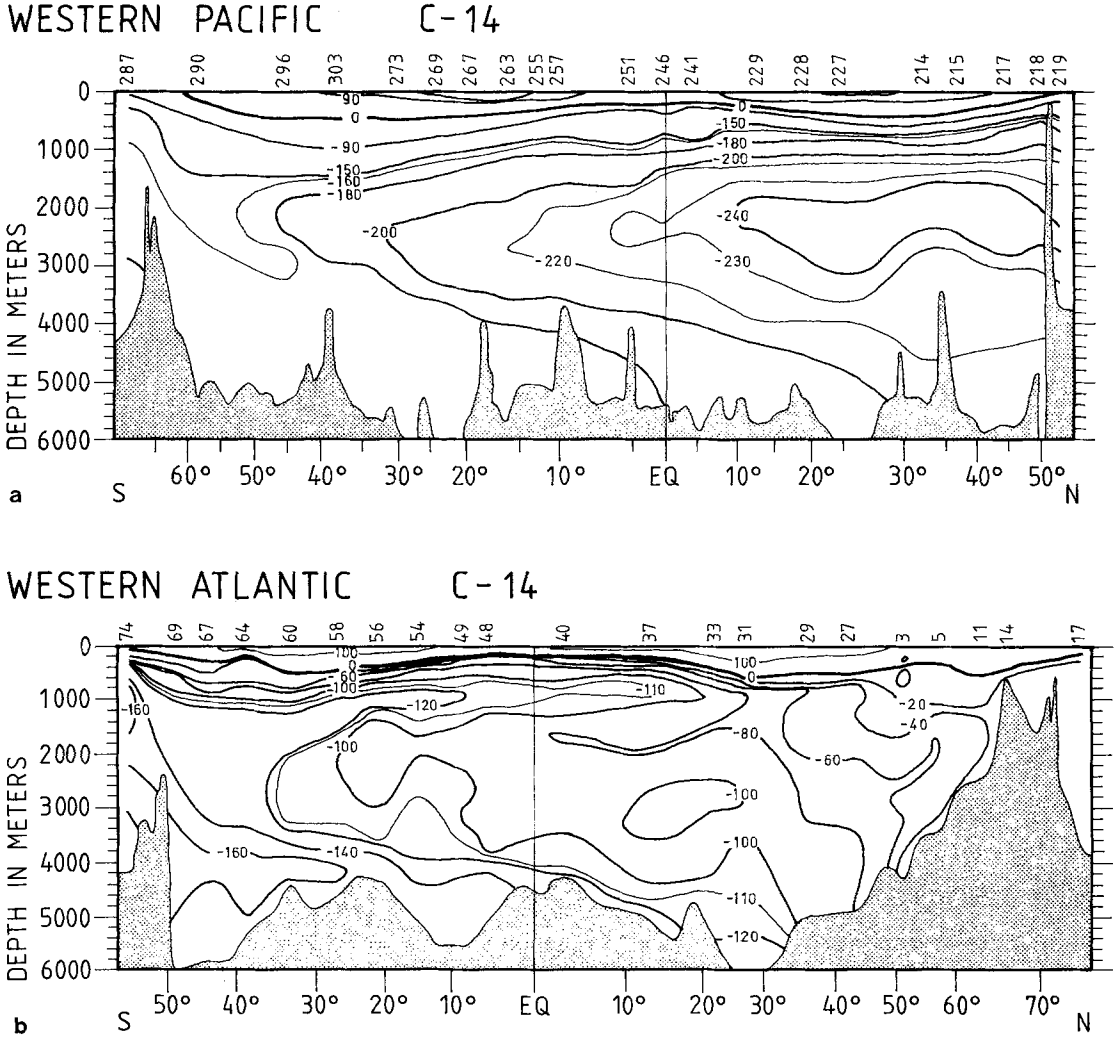

Fig. 12a and b. Observed $\Delta^{14}C$ distributions for the GEOSECS **a** Western Pacific and **b** Atlantic sections (after Stuiver and Östlund 1980; Östlund and Stuiver 1980)

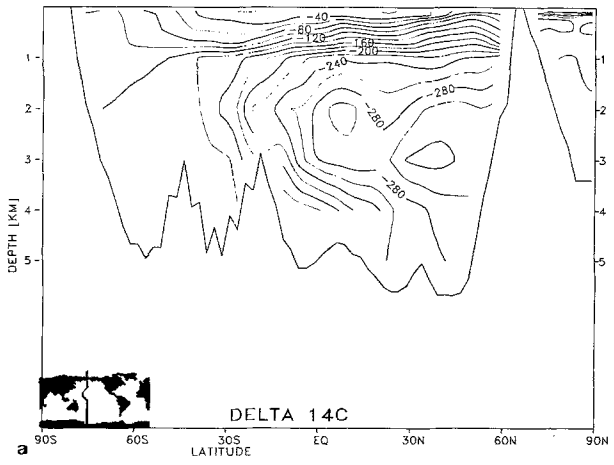

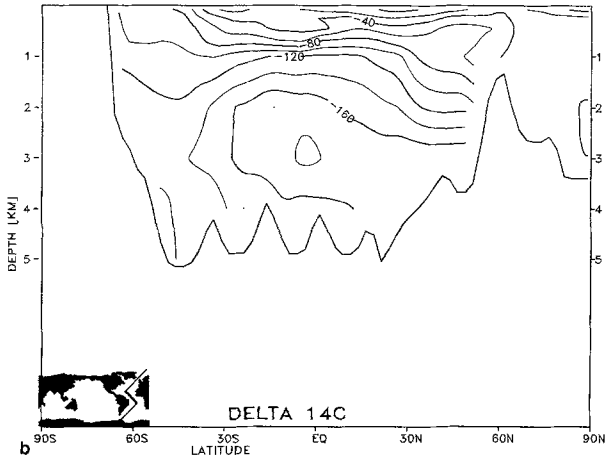

Fig. 13a and b. Model $\Delta^{14}C$ distributions corresponding to Fig. 12 with biological pump included (from BMR)

The carbon cycle model

The model was used to investigate both the ^{12}C cycle and — as a test of the long time-scale transport and residence time properties of the ocean model — the ^{14}C distributions discussed in the previous section.

We distinguish between the atmosphere, the uppermost (mixed) layer of the model in which chemical interactions take place, and the remaining interior ocean.

In the interior ocean, the carbon-related quantities are treated as tracers which are advected by the currents of the ocean circulation without sources or sinks. It is sufficient to keep track only of the total dissolved inorganic carbon C in the interior ocean, as this is the variable which determines the chemical equilibrium established in the mixed layer when the water mass returns to this layer.

The advection equation

$$\frac{\partial C}{\partial t} + u\nabla C = -rC, \tag{1}$$

where

$$r = \begin{cases} 0 & \text{for } ^{12}C \\ (8237.\text{year})^{-1} & \text{for } ^{14}C, \end{cases}$$

is solved numerically by an implicit upwind scheme

$$\frac{C^{t+\Delta t} - C^t}{\Delta t} + \sum_i u_i \frac{C_i^{t+\Delta t} - C^{t+\Delta t}}{\Delta x_i} = -rC^t \tag{2}$$

using a time step Δt of 1 year.

The summation index refers to the components of the current u and the C values at the corresponding adjacent upwind grid points in the three component directions. The numerical scheme is unconditionally stable and conserves carbon exactly for each carbon fraction. Equation (2) at each grid point defines a system of 27,443 coupled linear equations. The system is characterized by a well-conditioned, very sparse matrix, which can readily be solved by an iterative procedure. For our applications to rather slowly varying distributions, 8 iterations per year generally proved to be sufficient. The efficiency of the implicit scheme increases as one approaches the stationary state, and for the last 3000 years of a 4000-year run, convergence is normally achieved within round-off accuracy with only one iteration step.

Despite the need for an iteration cycle, the implicit scheme is more numerically efficient than a straightforward single-step forward integration method. To satisfy the CFL stability criterion for all grid points, a time step of about 1 week would be needed. (The Courant-Friederich-Levy condition ensures that the change in the inventory of a box in a time step, as computed from the flux budget, is less than the box inventory itself. It essentially implies that disturbances are not propagated more rapidly in the model than the true advection speed, i.e. that the effective displacement of a fluid particle in a time step is less than a grid cell dimension.) In practice, the critical regions of high velocities in which the horizontal or vertical

displacements of a fluid particle over 1 year exceed the grid cell dimension are limited to only very few grid points. Thus, a 1-year time step appears appropriate. In regions in which the advective displacements do exceed the cell dimension, the effect of the implicit scheme is to increase the numerical diffusion. This is probably not an unreasonable description of what really happens in regions of high currents, which are normally also associated with high temporal and spatial variability.

The atmosphere is represented simply as a highly diffusive layer providing the mean transport from warm regions of low solubility, where CO_2 evades from the ocean, to the cold regions of higher solubility, where the oceans absorb CO_2. The diffusion is limited to the meridional direction, complete mixing being assumed zonally. The diffusion equation is solved by a simple implicit scheme, which yields a tridiagonal matrix which can easily be inverted directly. The equivalent hemispheric mixing time scale of the atmosphere was chosen as 1 year. For our applications and time scales, the diffusion formalism represents only a minor modification over the treatment of the atmosphere simply as a single, instantaneously fully mixed box. A more realistic description of the atmospheric transport of CO_2 appropriate for seasonal time scales is given in Heimann et al. (subm. for publication).

The mixed layer is coupled to the interior ocean through the vertical upward or downward flux of total dissolved inorganic carbon at the bottom of the layer. This is determined by the vertical advection velocity at the bottom of the layer (and, at a few convectively unstable grid points, by vertical mixing at a rate determined by the mixing occurring in the dynamical circulation model).

The coupling of the mixed layer to the atmosphere occurs through the flux S of CO_2 through the air-sea interface, which is represented by the standard bulk formula

$$S=\lambda[(pCO_2)_o-(pCO_2)_a] \tag{3}$$

where the indices refer to the partial pressures of CO_2 in the atmosphere and the ocean, respectively. The bulk coefficient was chosen as $\lambda=0.05\ \text{mol m}^{-2}\text{a}^{-1}\ (\text{ppm})^{-1}$, corresponding to a gas exchange rate of $17\ \text{mol m}^{-2}\text{a}^{-1}$ for $pCO_2=340$ ppm (cf. Broecker, 1974). The value of λ, and its dependence on local environmental parameters such as wind speed, has been the subject of some discussion (cf. Brutsaert and Jirka, 1984), but in the present paper λ is kept constant. Further experiments to determine the sensitivity of our results with respect to a latitudinal dependence of λ, for example, would be of interest.

Equation (3) applies for ^{12}C, which alone determines the pCO_2 values due to the high abundance of ^{12}C relative to ^{14}C ($\approx 1:10^{-12}$). The corresponding equation for the ^{14}C flux, assuming that ^{14}C has the same fugacity as ^{12}C and that the carbon chemistry within the mixed layer determining the fractionation into different carbon constituents is the same for ^{12}C and ^{14}C, is given by

$${}^{14}S=\lambda\left[\left(\frac{^{14}C}{^{12}C}\right)_o (pCO_2)_o-\left(\frac{^{14}C}{^{12}C}\right)_a (pCO_2)_a\right]. \tag{4}$$

The fluxes of carbon through the top and bottom of the mixed layer and the divergence of the horizontal carbon transport within the layer determine the change of total carbon within a time step at any given grid point of the layer. Given the total carbon, pCO_2 and the other chemical concentrations in the mixed layer are computed from the chemical equilibrium equations for a seven-component system consisting of the three carbon components $[CO_2]$, $[HCO_3^-]$, $[CO_3^-]$, the borium components $[B(OH)_4^-]$, $[B(OH)_3]$ and the aqueous components $[H^+]$ and $[OH^-]$. The chemical equilibrium constants are taken from Millero (1978). The relation between pCO_2 and C is generally nonlinear and temperature dependent. Details are given in the Appendix.

In the numerical discretization of the mixed-layer density and flux balances, care must be taken with regard to the rather small time constant of the mixed layer relative to the atmospheric layer. To maintain numerical stability with a 1-year time step, an implicit time integration scheme was used. The CO_2 flux between the atmosphere and ocean required to determine the pCO_2 change occurring in the time step from t to $(t+\Delta t)$ was computed at time $(t+\Delta t)$. This is consistent with the implicit advection scheme (2) which was used to compute the remaining oceanic fluxes determining the mixed-layer carbon balance. The implicit equations were solved iteratively. The procedure requires solving for the full mixed-layer chemistry at each iteration step, since the pCO_2 values at time $(t+\Delta t)$ which determine the air-sea CO_2 flux must be computed from the total carbon C at time $(t+\Delta t)$ using the chemical interaction relations.

The steady-state equilibrium solution

Before applying the ocean carbon cycle model to CO_2 response problems, we test the ability of the model to reproduce the mean carbon distributions of the ocean. The initial values of the model run were adjusted such that the asymptotic equilibrium state was reasonably close to the assumed pre-industrial conditions, set as the year 1800. This steady state was then used later as the initial state for studying the time-dependent response to anthropogenic emissions. The asymptotic equilibrium pre-industrial state, attained after 4000 years of integration, yielded a mean atmospheric CO_2 concentration of 265 ppm [estimates of pre-industrial CO_2 values range between 250 and 290 ppm, cf. Bojkov (1983)].

Although, for the reasons stated earlier, the omission of biological processes in the present model is justified for studies of anthropogenically

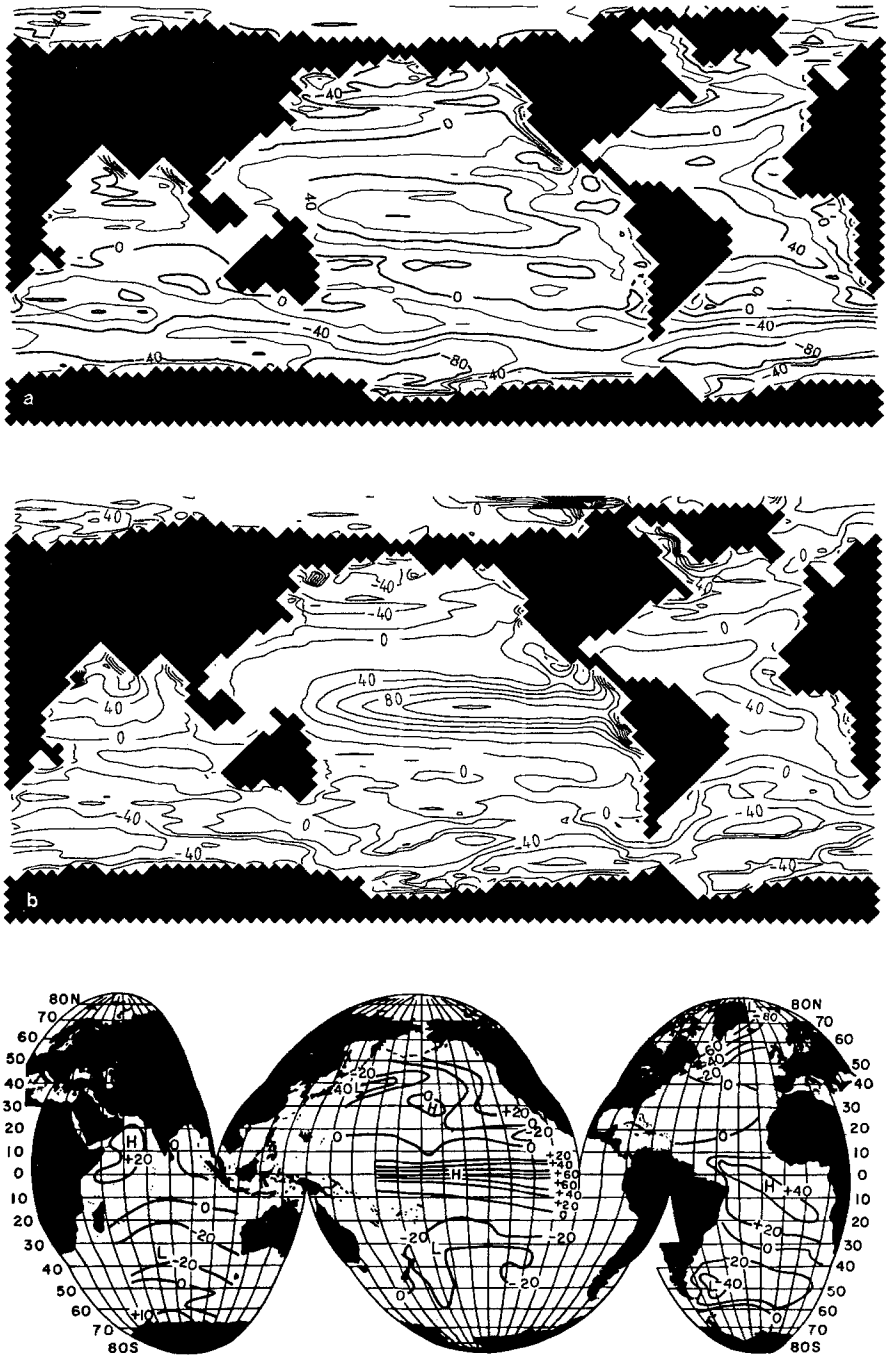

Fig. 14a—c. Ocean-atmosphere difference of pCO_2 computed by model **a** without biota and **b** with biota and **c** according to observations (from Takahashi et al. 1983), units in μbar

induced changes of ocean carbon concentrations, the biological pump is known to be an important factor in establishing the steady-state equilibrium distributions. It is thus of interest to compare the present inorganic model with the full model, including biota, of BMR.

Figure 14a, b and c shows a comparison of the difference $\delta(pCO_2)$ of the CO_2 concentration in the mixed layer and the atmosphere as inferred from observations (Takahashi et al. 1983) and as computed by both models. Vertical sections of total inorganic carbon for the Pacific and Atlantic oceans are shown in Figs. 15a, b, c and 16a, b, c. The agreement between observations and the full model is satisfactory (see BMR for a more detailed discussion). However, the inorganic model is also seen to capture some of the main features of the global ocean carbon distribution, namely

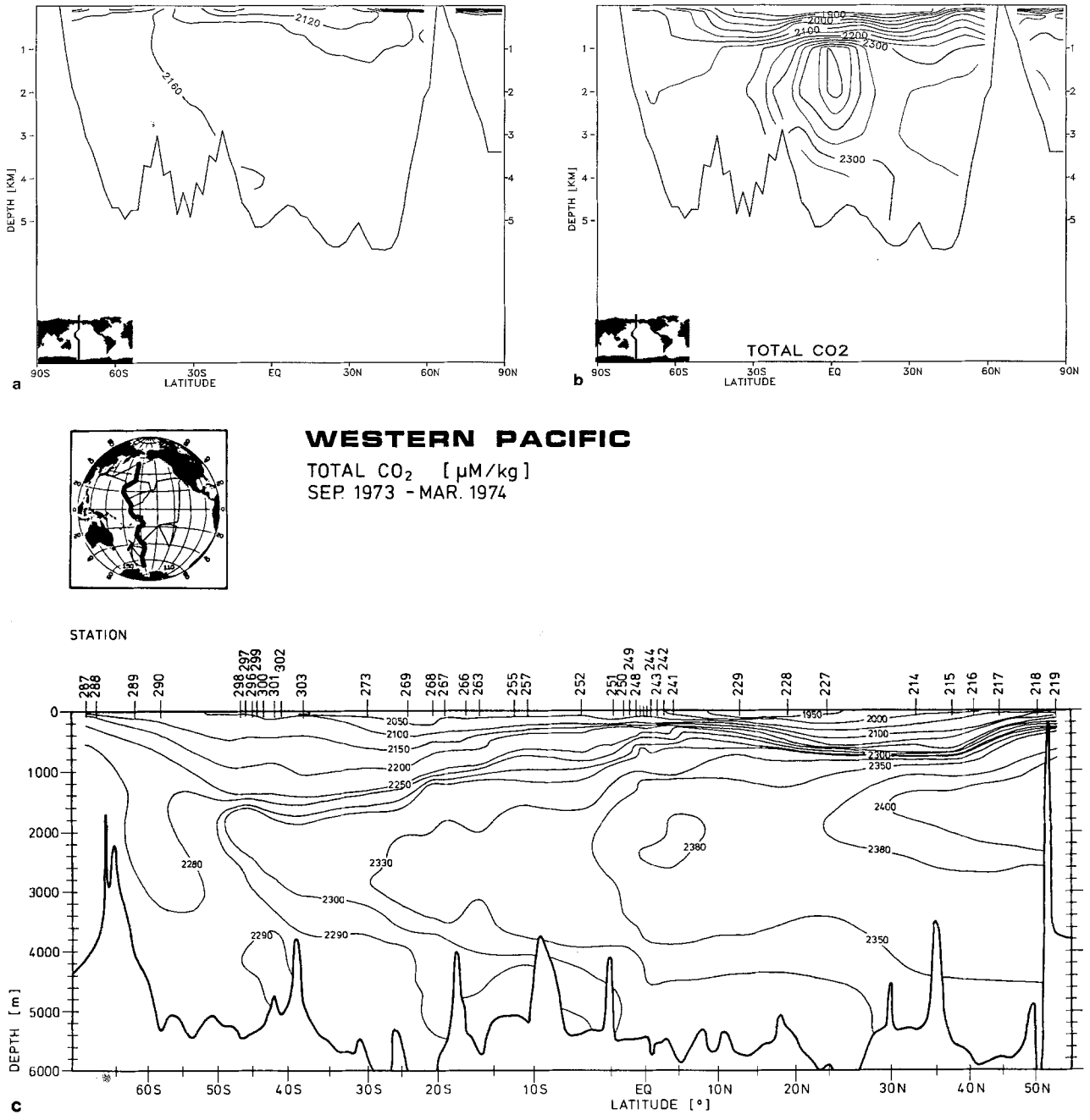

Fig. 15a—c. Western Pacific sections of total dissolved inorganic carbon (DIC) for models **a** without biota, **b** with biota and **c** as measured in GEOSECS (from Craig et al. 1981). Units are µmol/l

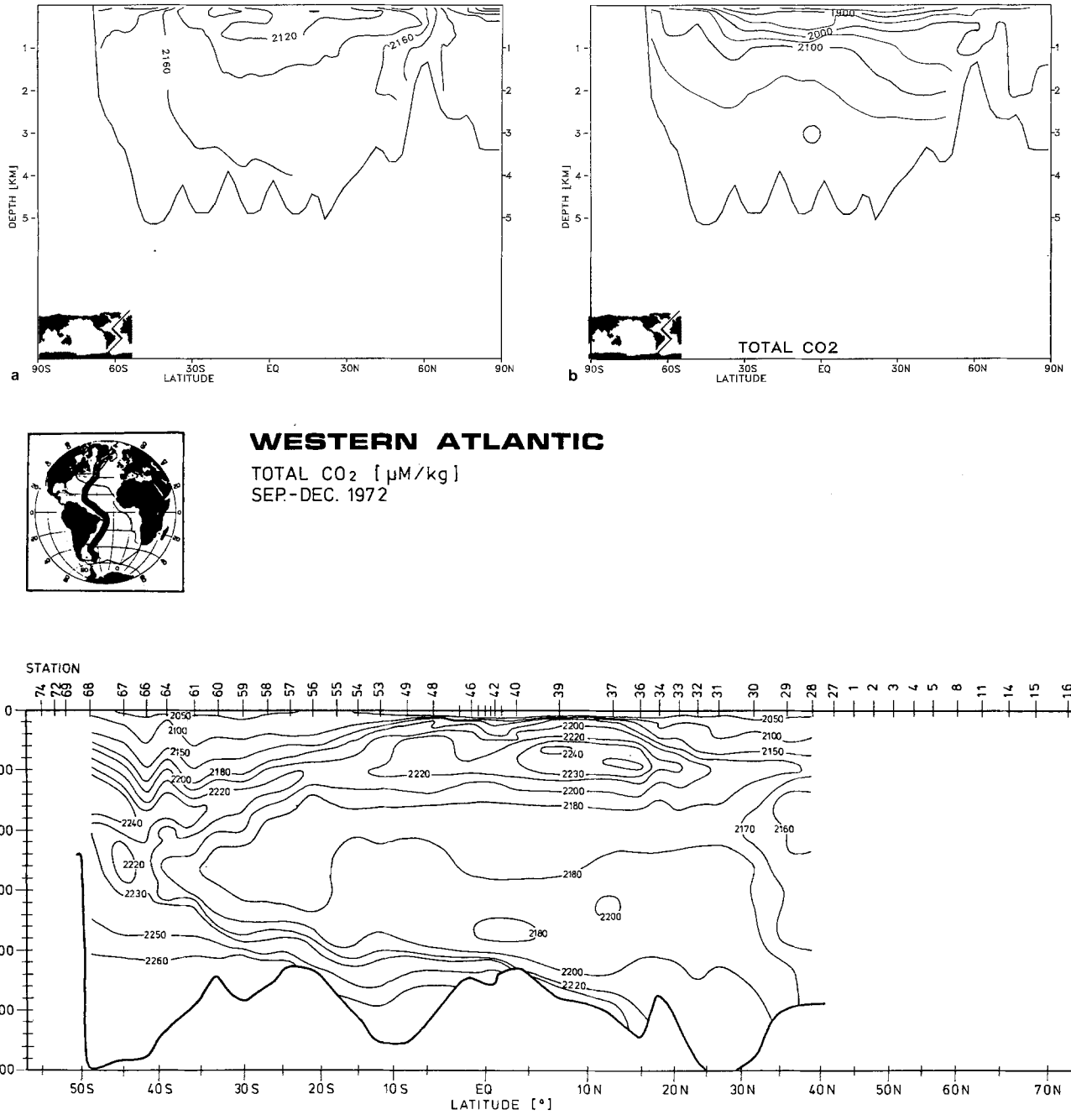

Fig. 16a—c. Same as Fig. 15 but for the Atlantic section (from Bainbridge A)

those which are governed by large-scale meridional overturning (cf. Fig. 6) and the equator-pole surface temperature gradient. At high latitudes, the larger CO_2 solubility of cold water results in a flux of CO_2 from the atmosphere into the ocean. The CO_2 is returned to the atmosphere in the equatorial regions, where the upwelling cold water becomes oversaturated on warming at the surface. The dominant influence of the temperature is apparent from the similarity of Fig. 14a with the (essentially observed) sea surface temperature distribution of Fig. 7. The large-scale equatorial-polar overturning structure of Fig. 6 is also clearly seen in the meridional sections, Figs. 15a and 16a.

The biological pump enhances these effects in upwelling regions, without significantly altering the basic pattern. The transport of particulate car-

bon downwards from the surface layers through biological activity and the subsequent release of carbon from the particulate form by remineralization increases the total dissolved inorganic carbon concentrations in the deeper layers of the ocean. In upwelling regions, such as the equator, these high concentration levels are carried up to the surface and magnify the positive pCO_2 amplitude in such regions by a factor of the order of 1.5.

We point out again that the operation of the biological pump remains practically unaffected by changes in the atmospheric CO_2 concentration, since the interaction rates are controlled by the nutrient cycle, independent of the interactions involved in the inorganic carbon cycle model.

Impulse response function

For small deviations about a stationary equilibrium state, the response of the coupled ocean-atmosphere carbon cycle to CO_2 input can be usefully summarized in terms of the linear impulse response (Green) function $G(t)$. This is defined as the CO_2 signal observed in the atmosphere for a δ-function atmospheric input at time $t=0$ (or equivalently a unit step-function change in the initial atmospheric CO_2 concentration). For times large compared with the atmospheric mixing time of the order of 1 year, the geographical distribution of the initial input pulse in the atmosphere is irrelevant. For an arbitrary emission function $x(t)$, the atmospheric CO_2 signal $y(t)$ is then given by

$$y(t)=\int G(t-t')x(t')dt'. \tag{5}$$

We assume that x and y are given in equivalent atmospheric pCO_2 units (1 GT atmospheric carbon ≈ 0.469 pCO_2). The function $G(t)$ can be determined by an appropriate step-function initial-value experiment with the full model. The simple form (5) can then be used for all subsequent numerical experiments with different input scenarios, provided the CO_2 changes remain in the linear range of the buffer factor.

The main advantage of the form (5) is, in fact, not so much the saving in computer time (a typical response run with the full model requires only 2 CPU min/century on a CYBER 205) as the insight it provides into the interplay of different characteristic relaxation times involved in the storage of CO_2 in the ocean. For this purpose it is useful to represent the function $G(t)$ (through a suitable fitting procedure) as a superposition

$$G(t)=A_0+\sum_j A_j \exp(-t/\tau_j) \tag{6}$$

of a number of exponentials of different amplitude A_j and relaxation time τ_j. The amplitude A_0 (≈ 0.15) represents the asymptotic airborne fraction for the equilibrium response of the ocean-atmosphere system to any finite-duration unit integral input function. The amplitudes A_j may be interpreted as the relative capacity of other reservoirs, which are filled up independently by the atmospheric input at rates characterized by the relaxation time scales τ_j. (The inclusion of a sedimentation sink in our model would yield a finite relaxation time also for the A_0 component, but this is at least an order of magnitude greater than the time scales considered here.) Mathematically, the individual exponentials may be regarded as eigen-modes of the system (cf. Sundquist 1985). In general, the full set of eigenvalues will normally contain modes with both complex and real eigenvalues, but in our empirical fitting procedure it was found that the Green function could be accurately represented using purely damped, non-oscillatory modes only.

Linear response expressions of the form (5) and (6) were least-square-fitted to the computed response of the full ocean carbon cycle model for three cases of a step-function initial change representing a sudden 25% increase, doubling and quadrupling, respectively, of the initial (1800) atmospheric CO_2 concentration $pCO_2=265$ ppm. The quadrupling experiment falls into the nonlinear response regime. However, an equivalent linear impulse response function expression was also fitted to the response for this case in order to estimate the changes induced in the effective relaxation times and amplitudes through the nonlinearities.

Figure 17 shows the decay of the atmospheric content with time for the three experiments. The model was integrated for 1000 years, which is still too short to reach a fully equilibrium response. However, the asymptotic equilibrium ratios $(\Delta pCO_2)_\infty/(\Delta pCO_2)_0$ can be computed theoretically (cf. Table 1) and are approximately 0.15 for all experiments. A very good fit, with residual errors which are undiscernible in Fig. 17, could be achieved for all curves with four exponentials (see Table 1). Also shown in Fig. 17 are the corresponding impulse response functions computed with the box-diffusion model of Siegenthaler (1983), using the parameters given by the author for the version of the model which was tuned to bomb ^{14}C data. The box-model response curves lie surprisingly close to the full model.

The rather small differences between the response functions for the first two experiments in-

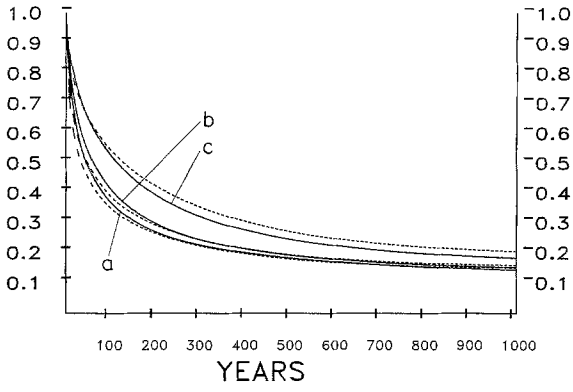

Fig. 17. Computed impulse response function for a step-function change of pCO_2 of 1.25 *(curve a)*, 2.0 *(curve b)*, and 4.0 *(curve c)*. *Dashed curves* show the corresponding response functions for the Siegenthaler and Oeschger (1978) box-diffusion model

dicate that the case of an initial doubling still lies fairly well within the linear regime. However, for an initial quadrupling, Table 1 shows significant changes in the fitted response function parameters. The main effect of the nonlinear increase of the buffer factor is to increase the net response time, as may be expected.

The representation of the impulse response function as a superposition (6) of exponentials with different relaxation times is particularly helpful in interpreting the different CO_2 storage properties of the oceans for different emission scenarios, as discussed in the following sections.

CO_2 increase during the period 1800—1984

The equivalent linear response function derived in the previous section should be fully applicable to the computation of the change of the atmospheric CO_2 concentration since the pre-industrial period, as the changes still lie well within the linear regime. However, as a check we have also determined the airborne fraction with the full model. The complete model, of course, also provides additional insight into the detailed spatial distribution of the carbon storage within the ocean.

The emission source function for the period 1800—1984 (Fig. 18, curve c) was constructed as a superposition of the CO_2 release through industrial activity (Fig. 18, curve a), taken from Rotty's (pers. comm.) compilation, and a biological source (Fig. 18, curve b) describing the effects of deforestation and changing land use. The biogenic input curve b is similar to the biogenic input estimated by Peng et al. (1983) [curve d, extended beyond 1965 in accordance with Edmonds et al. (1984)], but has been slightly modified as in Bojkov (1983) in order to be able to compare our model results with the analogous computations described in the World Climate Programme report WCP-53. The exact form of the biogenic in-

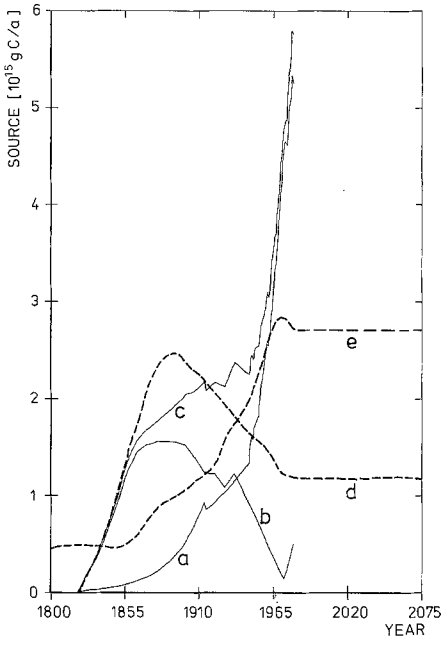

Fig. 18. CO_2 emission curves for the period 1800—1984. *Curve a:* industrial input according to Rotty (1981); *b:* biogenic input, as assumed in WCP-53 (1983); *c:* $a+b$, *d:* biogenic input according to Peng et al. (1983); *e:* biogenic input according to Houghton et al. (1984)

Table 1. Exponential fits to the computed impulse response function for step-function increases of the initial atmospheric pCO_2 by a factor of 1.25, 2 and 4, respectively

Step function	A_0	A_1	τ_1 [years]	A_2	τ_2 [years]	A_3	τ_3 [years]	A_4	τ_4 [years]
1.25	0.131	0.201	362.9	0.321	73.6	0.249	17.3	0.098	1.9
2	0.142	0.241	313.8	0.323	79.8	0.206	18.8	0.088	1.7
4	0.166	0.356	326.3	0.285	91.3	0.130	18.9	0.063	1.2

put is still uncertain, as evidenced by the alternative biogenic input proposed by Houghton et al. (1984), curve e [extended again in accordance with Edmonds et al. (1984) beyond 1965].

Figure 19 shows the evolution of the atmospheric pCO_2 computed both with the full model and the linearized impulse response function. As expected, the curves lie close together. A still closer agreement is found between the results for the full model and Oeschger's box model, which cannot be distinguished from the full model within the resolution of the curves. All three computations are based on the same net input source function (c) of Fig. 18. For reference, Oeschger's box-model reconstruction for the purely fossil-fuel input curve a, Fig. 18, is also shown.

Too much significance cannot be attached to the agreement between the computed atmospheric CO_2 content and the general level of the Mauna Loa curve, as the initial pre-industrial CO_2 level is uncertain to within ± 20 ppm, and suitable initial pCO_2 values and biogenic input curves can always be chosen such that the models come out at the Mauna Loa level. [Recent more accurate measurements in ice cores yield a pre-industrial pCO_2 value of 280 ± 10 ppm for 1860 (Neftel et al. 1985). Our curve lies within this interval and could in fact have been adjusted through a slight modification of the biogenic input to pass exactly through the 280-ppm value.] A critical comparison between observations and data can be based only on the increase in the CO_2 content between 1957 and 1986. It is of interest that both the present high-resolution carbon cycle model and the simpler box models yield a slightly too rapid atmospheric CO_2 increase during this period. Similar results with a number of other box models have led Killough and Emanuel (1981) to suggest that the biosphere may not have been releasing CO_2 during this period, as assumed in the present computations, but was in fact taking up CO_2. The implied uptake rates from the model calculations are of the order of 0.5 GT/year.

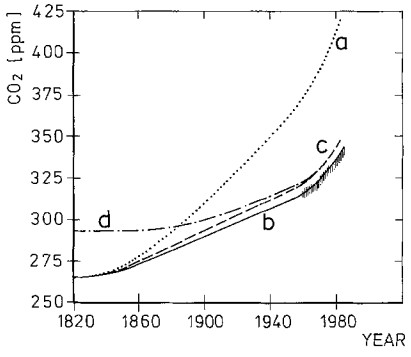

Fig. 19. Integrated input (*a*) and computed atmospheric CO_2 concentrations *(curves b, c)* for the period 1800—1984 for the input curve (*c*) of Fig. 18. *b:* full model and Oeschger's box model (indistinguishable in this diagram). *c:* impulse response function computation. *Curve d* is the atmospheric CO_2 concentration computed with Oeschger's box-diffusion model for an input consisting of an industrial source only (*curve a* of Fig. 18). Oeschger's box-model computations are from WCP-53, (1983)

Figures 20 and 21 show the changes of $\delta(pCO_2)$, the difference between the pCO_2 distribution in the surface layer and the atmospheric pCO_2, and total inorganic carbon which occurred in the surface layer between 1800 and 1984. The largest change is observed in the $\delta(pCO_2)$ distribution. The negative values reflect the lag of the pCO_2 increase in the ocean relative to the atmospheric pCO_2 increase due to the finite uptake time constant of the ocean. The largest lags, associated with the largest delay times, occur, as expected, in polar and upwelling regions. The equatorial high is reduced by 30%. The pattern of the change in total inorganic carbon, of the order of 2%—3%, is similar but not identical. This is due to the opposite temperature dependencies of the total C solubility which controls the C distribution, and the buffer factor which controls the $\Delta C/C$ pattern. The maximum solubility and therefore maximum C concentrations are found in the cold polar regions, whereas the maximum differential C uptake rates (minimum buffer factors) occur in the warmest regions of the ocean.

The vertical distribution of the computed change in total inorganic carbon between 1800 and 1984 is shown for the Western Pacific and Atlantic sections in Fig. 22. The ΔC distribution shows a general similarity to the tritium pattern of Fig. 10, although the time dependencies of the input source functions for the two experiments were quite different. Both experiments were, nevertheless, governed by similar 15- to 20-year time scales: in the case of tritium by the 15-year elapsed time since the approximate δ-function input in 1964; in the CO_2 case by the 20-year doubling time of the CO_2 emission rate. The time scales emphasize storage in the main thermocline region.

Figure 22 indicates that the deep ocean still has significant reserves for storing anthropogenic CO_2 emissions which have not been tapped in the past because of the rapid increase in the CO_2 emission rates. As pointed out by Siegenthaler and Oeschger (1978) and others, and discussed further

Fig. 20. Change in ocean-atmosphere difference $\delta(pCO_2)$ between 1800 and 1984. Units are μbar

Fig. 21. Change in total dissolved inorganic carbon in surface layer between 1800 and 1984. Units are μmol/C

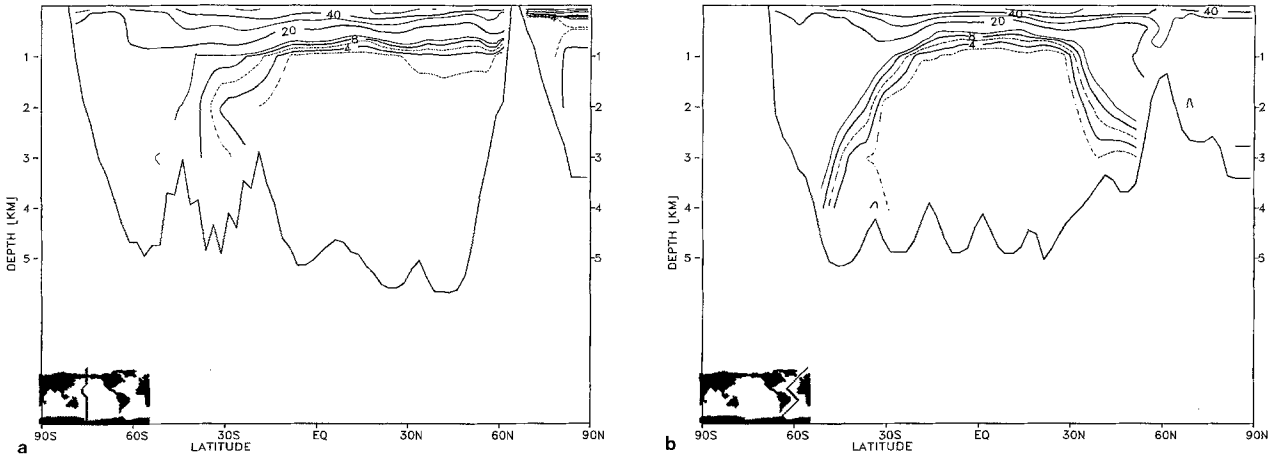

Fig. 22a and b. Vertical sections of relative change ΔC of total inorganic carbon between 1800 and 1984 for **a** Western Pacific and **b** Atlantic

in the following section, a reduction of CO_2 emissions would therefore not only slow down the increase of total carbon in the system, but would also reduce the fraction remaining in the atmosphere by enabling the deep ocean to take up a larger proportion of the total increase.

The sources of ^{14}C during the last century differ significantly from the ^{12}C input. Up to 1950, the ^{14}C fraction in the atmosphere must have decreased continuously dut to the input of aged fossil-fuel carbon. The nuclear weapons tests in the 1950s and early 1960s then released a substantial amount of ^{14}C. This input has the same time dependence as the tritium input, but the regional distribution is much more uniform.

The dilution of ^{14}C through fossil-fuel burning was computed using Rotty's input curve, curve a, Fig. 18. The bomb ^{14}C input was modelled by simply prescribing the atmospheric ^{14}C concentration as observed by Nydal and Lövseth (1983) after 1961. This avoids problems of determining the uptake of bomb ^{14}C by the terrestrial biosphere. Figure 23 shows the total ^{14}C sections for the Pacific and Atlantic (to be compared with the GEOSECS 1973 section in Fig. 12) and the corresponding sections of the difference $(\Delta^{14}C)_{1973} - (\Delta^{14}C)_{1820}$ (which may be compared with the tritium sections).

In contrast to tritium, which was inserted almost solely in the Northern Hemisphere, the Antarctic deep convection system is very effective in transferring ^{14}C to the deep ocean. The observed penetration is fairly well reproduced in the Southern Ocean, whereas in the Northern Atlantic the agreement is again only qualitative, for the same reasons as discussed for the tritium distributions.

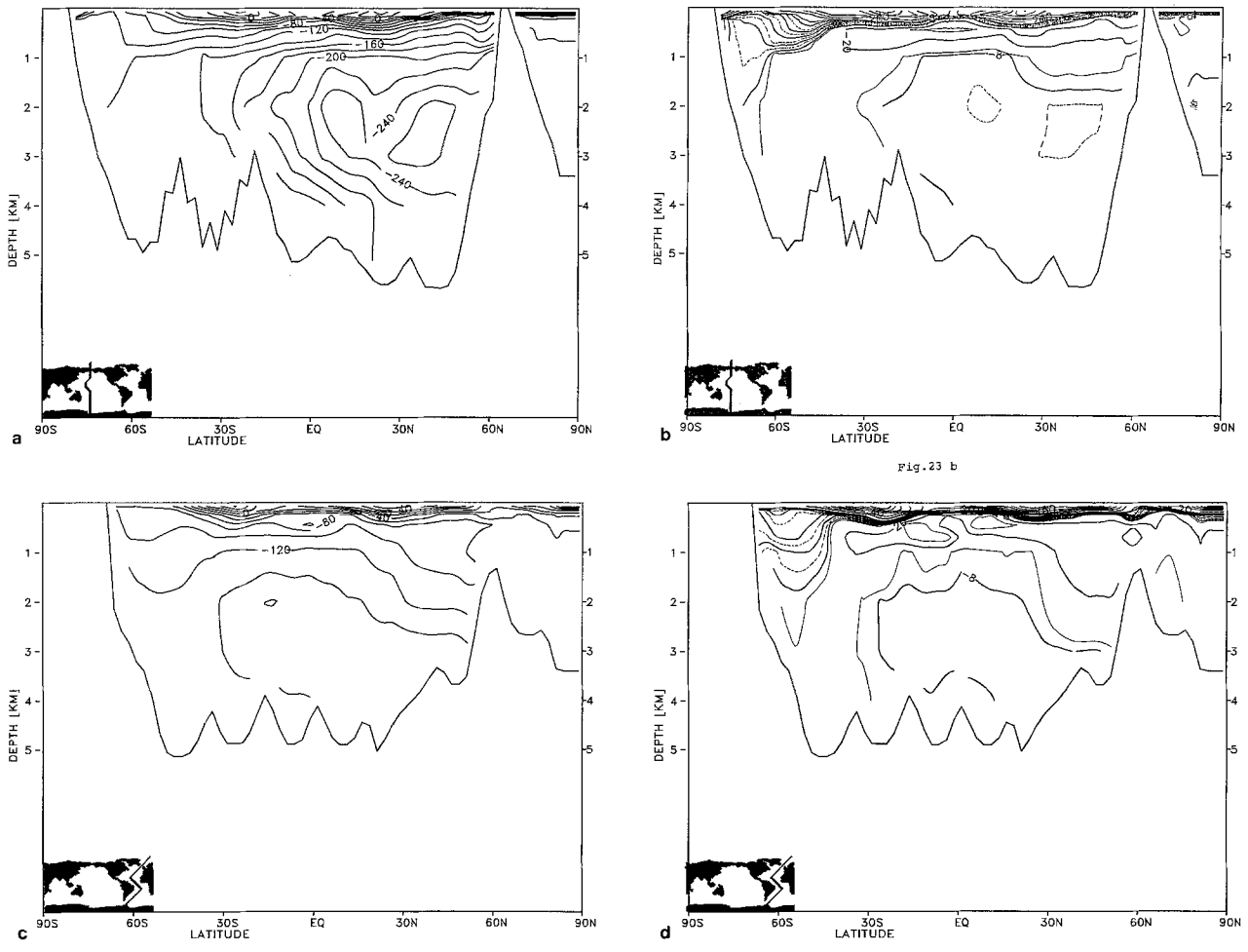

Fig. 23a—d. Computed $\Delta^{14}C$ distributions in the ocean for 1973. The deviation from the pre-industrial equilibrium in 1820, Fig. 11, arises from the fossil-fuel input, which was taken as Rotty's curve (a), Fig. 18, and the bomb ^{14}C input, which was introduced by prescribing the atmospheric ^{14}C concentrations in accordance with the observations of Nydal and Lövseth (1983) after 1961. **a:** $(\Delta^{14}C)_{1973}$, Pacific section; **b:** $(\Delta^{14}C)_{1973} - (\Delta^{14}C)_{1820}$, Pacific section; **c, d:** same as **a, b** for Atlantic section

Future CO_2 emission scenarios

The equivalent linear impulse response function introduced earlier is a particularly convenient tool for rapidly computing the future atmospheric CO_2 concentrations for a variety of different CO_2 emission scenarios. However, it should be used with caution in these applications, as the predicted CO_2 levels often lie outside the linear regime of the carbon model. We shall therefore again carry out computations using both the linear response model approximation and the full carbon cycle model.

An advantage of the equivalent linear response model is that the response of the atmospheric CO_2 concentration can be given analytically for simple classes of emission functions (Table 2). An inspection of Table 2 reveals the following basic properties of the response:

i) For a constant or linear emission function, the response is dominated asymptotically by the quasi-equilibrium term A_0 of the response function. Thus the airborne fraction approaches 15% for large t.

ii) For a more rapid, exponential increase of the emission, all response terms contribute asymptotically to the exponential response. The individual response terms are weighted by the factors $w_j = \tau_e \tau_j/(\tau_e + \tau_j)$, where τ_e is the input e-folding time.

iii) For the large time-constant terms $\tau_j \gg \tau_e$, $w_j \approx \tau_e$ (this includes formally the component $j=0$, for which $\tau_j = \infty$). Thus, the net asymptotic response

$$y_{lt}(t) = \left(\sum_{j(\tau_j \gg \tau_e)} A_j \right) \tau_e e^{-t/\tau_e}$$

for the long time-constant components of the signal is given simply by the integrated response of an atmosphere which has no transfer loss to the ocean (reduced by the factor A_j characterizing the relative contributions of these terms to the total response).

iv) For the fast response components, $\tau_j \ll \tau_e$, on the other hand, the response amplitudes are reduced by the factor τ_j/τ_e. Thus, for small τ_j the contribution from these terms to the airborne fraction can be ignored — the equilibration with the oceans is achieved within the emission characteristic time scale τ_e for these components, and the airborne fraction is reduced accordingly.

The differences in response behaviour for different time-scale regimes affect the CO_2 projections for alternative emission scenarios. Past anthropogenic emission rates have been characterized by exponential growth with e-folding times of the order to 20—40 years. In this case the response terms associated with time constants of the order of the deep-ocean residence time do not contribute significantly, and the ocean uptake, of the order of 40% of total emissions, is determined by the relatively small mixed-layer and main thermocline reservoirs. However, if the emission growth rate is slowed down to time scales in the range of the deep-ocean circulation time, the larger deep-ocean reservoir comes into play, and the airborne fraction is reduced accordingly. If the input growth rate is reduced still further from an exponential to a power law, the response is dominated asymptotically by the quasi-equilibrium term A_0, and the airborne fraction approaches 15%. (The instantaneous airborne fraction can, in fact, become even smaller than this equilibrium fraction if the emission rate is decreased exponentially. In this case the ocean contains a disproportionately high fraction of dis-

Table 2. Response relations for simple input source functions

	Emission function $x(t)$	Atmospheric CO_2 response $y(t)$ (initial value 0 for $t=0$)
δ-function:	$\delta(t)$	$A_0 + \sum_j A_j \cdot e^{-t/\tau_j}$
constant:	C	$C[A_0 t + \sum_j A_j \tau_j (1 - e^{-t/\tau_j})]$
linear increase:	Bt	$B\left[A_0 \frac{t^2}{2} + \sum_j A_j \tau_j \{t - \tau_j (1 - e^{-t/\tau_j})\}\right]$
exponential increase: (decay for $\tau_e < 0$)	De^{t/τ_e}	$D\left[A_0 \tau_e (e^{t/\tau_e} - 1) + \sum_j A_j \left(\frac{\tau_e \tau_j}{\tau_e + \tau_j}\right)(e^{t/\tau_e} - e^{-t/\tau_j})\right]$

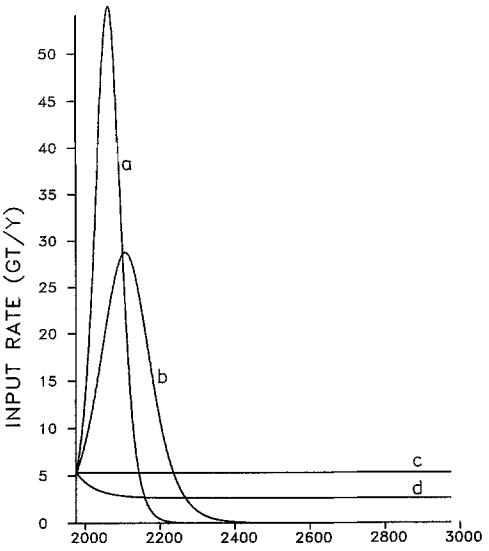

Fig. 24. Emission scenarios corresponding to logistic input functions with two different time scales *(curves a and b)*, a constant input at present-day levels *(curve c)* and an exponentially decreasing input up to the year 2018, succeeded by a constant input at half the present-day level *(curve d)*

solved carbon absorbed from earlier periods of higher atmospheric concentrations.)

Figure 25 shows the atmospheric CO_2 concentrations and airborne fractions computed with the linearized and full model for four different emission scenarios, presented in Fig. 24. The first two cases correspond to logistic input functions

$$\frac{dQ}{dt} = \mu Q\left(1 - \frac{Q}{R}\right) \tag{7}$$

following Killough and Emanuel (1981) [see also Bacastow and Björkström (1981), and Laurmann and Rotty (1983), for slightly modified forms]. Here Q is the sum of all fossil fuel, exploited up to time t, and R is the total reservoir of exploitable fuel. For case (a) we have assumed $\mu = 4.3\%$/year (corresponding to the pre-oil-crisis emission growth before 1973), $R = 5{,}000$ GT, while for case (b) the value $\mu = 2.35\%$/year (corresponding to the last decade) was taken, with the same value for R. In both cases the initial (present) value of Q is chosen such that $dQ/dt = 5.2$ GT/year. Case (c) corresponds to a constant emission function equal to the present value, while case (d) corresponds to an exponentially decreasing emission function with a half-life of 34 years (2% decrease per year) reaching a constant emission rate of 2.6 GT/year thereafter. None of the emission functions correspond exactly to the pure cases listed in Table 2. [Cases (c) and (d) differ from these cases because of the different initial conditions resulting from different pre-initial emission functions.] However, the different response properties corresponding to different time-scale regimes are clearly discernible, including the over-proportional reduction in the airborne fraction achieved by a reduction in the emission growth rate.

The response curves computed with the linearized input response functions are seen to be reasonably accurate for small pCO_2 changes, but significantly underestimate the amplitude and time scale of the airborne fraction in the nonlinear regime.

Conclusions

The purpose of this study was to gain a first insight into the problems of simulating the CO_2 storage properties of the ocean using a full 3 d ocean circulation model. Ocean biota were not included. To first order, the biological cycle does not affect changes in CO_2 storage induced only by external changes in CO_2 emissions without accompanying changes in the ocean circulation or other climatic factors. A full treatment of all climatic feedbacks accompanying a CO_2 increase requires, of course, more complete carbon cycle models as described in BMR and Esser G et al. (in prep.). However, a number of interesting conclusions can be derived with the present model:

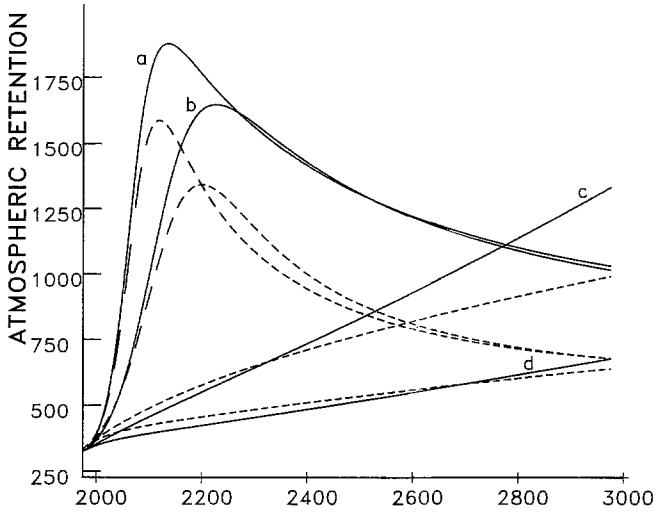

Fig. 25. Atmospheric CO_2 concentrations (ppm) for the four emission scenarios of Fig. 24 computed with the full model *(full curves)* and the equivalent linear input response function method *(dotted curves)*. The linear input response function is seen to underestimate the amplitude and time scale of the response for higher pCO_2 levels, but is a good approximation for small changes

1) The model yields a reasonable simulation of the quasi-stationary present-day horizontal distribution of carbon in the ocean. In particular, the large-scale structure of the observed pCO_2 distribution of the surface layer of the ocean is reproduced satisfactorily. This is governed by a combination of the regional distribution of the surface temperature, the large-scale overturning of the ocean and the temperature-dependent chemistry in the surface layer which determines the effective buffer factor. However, the maximal $\delta(pCO_2)$ values in local regions of strong upwelling along coasts and near the equator are underestimated by factors up to 1.5 relative to the full model of Bacastow and Maier-Reimer including the biological pump. The sub-surface carbon maxima also cannot be simulated by a model without biota.
2) The effective CO_2 linear impulse response function of the model exhibits a multi-time-scale structure, as expected on the basis of the known multi-time-scale structure of the ocean circulation. A relatively good analytical approximation to the computed impulse response can be given in terms of a superposition of a relatively small number (~ 4) of exponential functions. The response curves agree rather closely with Siegenthaler and Oeschger's (1978) results for a box-diffusion model. Thus (properly tuned) box models can still be usefully applied for first-order CO_2 scenario studies not concerned with the feedback of climatic changes on the carbon cycle.
3) The CO_2 response is nonlinear through the nonlinearity of the chemical interaction rates in the surface layer. Increasing CO_2 concentrations yield increasing buffer factors and thus a reduction of the oceanic CO_2 uptake (as discussed already for box models). The nonlinearity limits the applicability of the equivalent linear response function representation to CO_2 concentration increases of less than a factor of the order of two.
4) Projections of future atmospheric CO_2 concentrations for different emission scenarios demonstrate the importance of determining the detailed time history of the oceanic CO_2 response function. As has been concluded already from box-model computations, a significant decrease in the airborne fraction can be achieved by slowing down the emission rates so that the deeper ocean layers have time to absorb a larger fraction of the total emissions. It is hoped that the present model will provide an improved tool for carrying out detailed qualitative computations of such effects.
5) The present ocean CO_2 model contains no tunable parameters beyond those already introduced into the dynamical ocean circulation model (and the CO_2 surface flux boundary condition). In the present advective circulation model, these involve essentially only the convective adjustment mechanism and the momentum, heat and moisture fluxes at the air-sea interface, which are treated by standard methods. The tests with the model described in this paper thus provide some confidence for future applications of the model in climate feedback studies involving changes in both the ocean circulation and CO_2 distributions.

References

Bacastow R, Björkström A (1981) Comparison of ocean models for the carbon cycle. In: Bolin B (ed) Carbon cycle modelling, SCOPE 16:29—80. John Wiley and Sons, New York

Bainbridge A GEOSECS ATLANTIC EXPEDITION, Sections and profiles. Washington

Berger WH, Keir RS (1984) Glacial-holocene changes in atmospheric CO_2 and the deep-sea record. In: Hansen JE, Takahashi T (eds) Climate processes and climate sensitivity. AGU, Washington DC, 337—351

Berner WI, Stauffer B, Oeschger H (1979) Past atmospheric composition and climate. Gas parameters measured on ice cores. Nature 275:53—55

Björkström A (1979) A model of CO_2 interaction between atmosphere, oceans and land biota. In: Bolin B, Degens ET, Kempe S, Ketner P (eds) The global carbon cycle. SCOPE 13:403—457. John Wiley and Sons, New York

Bojkov RD (ed) (1983) Report of the WMO (CAS) meeting of experts of the CO_2 concentrations from pre-industrial times to IGY. WCP-53, WMO, Geneva

Bolin B (1975) A critical appraisal of models for the carbon cycle. In: The physical basis of climate and climate modeling, GARP Publ. No 16:225—235

Bolin B, Eriksson E (1959) Changes in the carbon dioxide content of the atmosphere and sea due to fossil fuel combustion. In: The Rossby Memorial Volume, New York, 130—142

Bolin B, Degens ET, Kempe S, Ketner P (eds) (1979) The global carbon cycle, SCOPE 16, John Wiley and Sons, New York

Broecker WS (1974) Chemical oceanography. 214 pp, Harcourt Brace Jovanovich, NY

Broecker WS, Takahashi T (1984) Is there a tie between atmospheric CO_2-content and ocean circulation? In: Hansen JE, Takahashi T (eds) Climate processes and climate sensitivity. Geophys Monogr Ser 29:314—326. AGU, Washington DC

Brutsaert W, Jirka GH (eds) (1984) Gas transfer at water surfaces. 639 pp, Reidel Publ, Dordrecht Boston Lancaster

Bryan K (1969) Climate and the ocean circulation. III. The ocean model. Mon Wea Rev 97:806—834

Bryan K (1979) Models of the world ocean. Dyn Atmosph Oceans 3:327—338

Bryan K, Lewis LJ (1979) A water mass model of the world ocean. J Geophys Res 84:2503—2517

Bryan K, Spelman MT (1986) The oceanic response to a CO_2 induced warming. J Geophys Res 90, C6:11679—11688

Craig H, Broecker WS, Spencer D (1981) GEOSECS PACIFIC EXPEDITION, Sections and profiles, Washington

Delmas RJ, Ascencio J-M, Legrand M (1980) Polar ice evidence that atmospheric CO_2 29,000 yr. BP was 50% of the present. Nature 284:155—157

Edmonds JA, Reilly T, Trabalka TR, Reichle D-E (1984) An analysis of possible future atmospheric retention of fossil fuel CO_2. Dept Energy, DOE/OR21400-1

Hasselmann K (1982) An ocean model for climate variability studies. Progr Oceanogr 11:69—92

Hellermann S (1967) An updated estimate of the wind stress on the world ocean. Mon Weather Rev 95:593—606

Houghton RA, Hobbie JE, Melillo JM, Moore B, Peterson BJ, Shaver GR, Woodwell GM (1984) Changes in the carbon content of terrestrial biota and soils between 1860 and 1980: A net release of CO_2 to the atmosphere. Ecol Monogr 53:235—262

Keeling CD (1973) The carbon dioxide cycle: reservoir models to depict the exchange of atmospheric carbon dioxide with the oceans and land plants. In: Rasool SI (ed) Chemistry of the lower atmosphere. Plenum Press, NY 251—328

Keeling CD, Bacastow RB, Whorf TP (1982) Measurements of the concentration of carbon dioxide at Mauna Loa Observatory, Hawaii. In: Clark WC (ed) Carbon Dioxide Review, 377—385

Killough GG, Emanuel WR (1981) A comparison of several models of carbon turnover in the ocean with respect to their distributions of transit time and age, and responses to atmospheric CO_2 and ^{14}C. Tellus 33:274—290

Lal D, Suess HE (1983) Some comments on the exchange of CO_2 across the air-sea interface. J Geophys Res 88, C6:3643—3646

Laurmann JA, Rotty RM (1983) Exponential growth and atmospheric carbon dioxide. J Geophys Res 88, C2:1295—1299

Levitus S, Oort AH (1977) Global analysis of oceanographic data. Bull Am Met Soc 58:1270—1284

Maier-Reimer E (1984) Towards a global ocean carbon model. Progress in Biometeorology 3:295—310

Maier-Reimer E, Hasselmann K, Olbers D, Willebrand J (1982) An ocean circulation model for climate studies. Techn. Report, Max-Planck-Institut für Meteorologie, Hamburg

Millero FJ (1978) The thermodynamics of the carbonate system in sea water. Geoch et Cosmoch Acta 43:1651—1661

National Academy of Sciences (1982) Carbon dioxide and climate: a second assessment. Report of the CO_2/Climate Review Panel, National Research Council, Acad Press, Washington DC

Neftel A, Moor E, Oeschger H, Stauffer B (1985) Evidence from polar ice cores for the increase in atmospheric CO_2 in the past two centuries. Nature 315:45—47

Neftel A, Oeschger H, Schwander J, Stauffer B (1983) Carbon dioxide concentration in bubbles of natural cold ice. J Phys Chem 87:4116—4120

Nydal R, Lövseth K (1983) Tracing bomb ^{14}C in the atmosphere 1962—1980. J Geophys Res 88, C6:3621—3642

Oeschger H, Siegenthaler U, Schotterer U, Gugelmann A (1975) A box diffusion model to study the carbon dioxide exchange in nature. Tellus 27:168—192

Östlund HG, Stuiver M (1980) GEOSECS Pacific radiocarbon. Radiocarbon 22:25—53

Östlund HG, Dorsey HG, Brescher R (1976) GEOSECS Atlantic radiocarbon and tritium results (Miami). Tritium Laboratory Data report no. 5, Rosenstiel School of Marine and Atmospheric Science, Univ. of Miami

Peng TH, Broecker WS, Freyer HD, Trumbore S (1983) A deconvolution of the tree-ring based $\delta^{13}C$ record. J Geophys Res 88, C6:3609—3620

Revelle R, Suess HE (1957) Carbon dioxide exchange between atmosphere and ocean and the question of an increase of atmospheric CO_2 during the past decades. Tellus 9:18—27

Riley JP, Skirrow G (1965) Chemical oceanography, Vol. I, 712 pp, Vol. II, 508 pp. Academic Press, London NY

Rotty RM (1981) Data for global CO_2 production from fossil fuels and cement. In: Bolin (ed) Carbon cycle modelling, SCOPE 16:121—127. John Wiley and Sons, New York

Rotty RM (1983) Distribution of and changes in industrial carbon dioxide production. J Geophys Res 88, C2:1301—1308

Rotty RM (1986) A look at 1983 CO_2 emissions from fossil fuels (draft manuscript)

Siegenthaler U (1983) Uptake of excess CO_2 by an outcrop-diffusion model of the ocean. J Geophys Res 88, C6:3599—3608

Siegenthaler U, Oeschger H (1978) Predicting future atmospheric carbon dioxide levels. Science 199:388—395

Stuiver M, Östlund HG (1980) GEOSECS Atlantic radiocarbon. Radiocarbon 22:1—24

Sundquist ET (1985) Geological perspectives of carbon dioxide and the carbon cycle, 5—59. In: Sundquist ET, Broecker WS (eds) The carbon cycle and atmospheric CO_2: natural variations Archean to present. Am Geophys Union, Washington DC, 627 pp

Sundquist ET, Broecker WS (eds) (1985) The carbon cycle and atmospheric CO_2: natural variations Archean to present. Am Geophys Union, Washington DC, 627 pp

Takahashi T, Chipman D, Volk T (1983) Geographical, seasonal and secular variations of the partial pressure of CO_2 in surface waters of the North Atlantic Ocean: the results of the North Atlantic TTO Program. In: Proceedings of the Carbon Dioxide Research Conference, Washington DC, Department of Energy, Cof.-820970, II.123—II.145

Viecelli IA, Elsaesser HW, Burt IE (1981) A carbon cycle model with latitude dependence. Climatic Change 3:281—301

Weiß W, Roether W (1980) The rates of tritium input to the world oceans. Earth Planet Sci Lett 49:435—446

Received September 8, 1986/Accepted January 23, 1987

Appendix

Mechanism of CO_2 buffering

For the chemistry of the mixed layer we consider the four most important (inorganic) interactions (cf. Riley and Skirrow, 1965)

$$H_2O + CO_2 \rightarrow H^+ + HCO_3^- \tag{8}$$

$$HCO_3^- \rightarrow H^+ CO_3 \tag{9a}$$

or

$$H_2O + CO_2 \rightarrow 2H^+ + CO_3^{--} \tag{9b}$$

$$H_2O \rightarrow H^+ + OH^- \tag{10}$$

$$H_2OB(OH)_3 \rightarrow H^+ + B(OH)_4^- . \tag{11}$$

The four mass balance equations for these interactions, together with the conservation equations for the four elements C, H, O and B occurring in the interactions, yield eight equations for the eight unknown constituent concentrations. The system also conserves charge. However, this is not an independent condition needed to specify the equilibrium state, but can be recovered as a linear combination of the four individual element conservation equations.

Since the concentration of H_2O is much higher than that of the other constituents, this term may be regarded as effectively constant in the mass balance equations, in which only the fractional concentration changes enter. However, the changes of $[H_2O]$ cannot be disregarded in the conservation equations, for which the absolute incremental changes are relevant. To remove $[H_2O]$ from further analysis, the term must therefore be eliminated from the two conservation equations for H and O in which this constituent appears. This is most easily achieved by replacing the H and O conservation equations by the single equation for the conservation of charge, or 'alkalinity'

$$A = 2[CO_3^{--}] + [HCO_3^-] + [OH^-] + [B(OH)_4^-] - [H^+] = \text{constant} \tag{12}$$

in which $[H_2O]$, as a neutral constituent, does not appear.

The residual seven-component system is then determined by the three conservation equations for alkalinity A, Eq. (12), total borate

$$B_t = [B(OH)_3] + [B(OH)_4^-] = \text{constant}, \tag{13}$$

total carbon

$$C = [CO_2] + [HCO_3^-] + [CO_3^{--}] \tag{14}$$

and the four mass balance equations

$$[H^+][HCO_3^-] = K_1[CO_2] \tag{15}$$

$$[H^+]^2[CO_3^{--}] = K_2[CO_2] \tag{16}$$

$$[H^+][OH^-] = K_w \tag{17}$$

$$[H^+][B(OH)_4^-] = K_B[B(OH)_3] \tag{18}$$

where the constant concentration $[H_2O]$ has been absorbed in the mass balance coefficients K_1, K_2 and K_w.

The concentration $[CO_2]$ determines the CO_2 partial pressure in the ocean through the relation $(pCO_2)_0 = [CO_2]/\alpha$, where α is the solubility of CO_2 in sea water.

Eliminating all constituents except $h = [H^+]$ and $s = [CO_2]$ with the aid of Eq. (13), (15) and (18), the system can be reduced to the pair of equations

$$C = \left(1 + \frac{K_1}{h} + \frac{K_1 K_2}{h^2}\right) s \tag{19}$$

$$A = s\left(1 + \frac{K_1}{h} + 2\frac{K_1 K_2}{h^2}\right) + \frac{K_w}{h} + \frac{B_t}{\left(1 + \frac{h}{K_b}\right)} - h. \tag{20}$$

To determine the variations in equilibrium concentrations associated with a variation dC in the prescribed total carbon content, we consider the differential forms

$$dC = \frac{\partial C}{\partial s} ds + \frac{\partial C}{\partial h} dh \tag{21}$$

and

$$dA = \frac{\partial A}{\partial s} ds + \frac{\partial A}{\partial h} dh. \tag{22}$$

Since the total carbon is changed only through the flux of charge-free CO_2 through the air-sea interface, we have $dA = 0$ and thus

$$dh = -\frac{\partial A}{\partial s}\left(\frac{\partial A}{\partial h}\right)^{-1} ds \tag{23}$$

and

$$dC = ds\left[\frac{\partial C}{\partial s} - \frac{\partial C}{\partial h}\frac{\partial A}{\partial s}\left(\frac{\partial A}{\partial h}\right)^{-1}\right]. \tag{24}$$

The above derivation follows Bolin and Eriksson (1959), with appropriate generalization to include the aqueous and borate system. Equations (19) and (20) yield the inequalities

$$\frac{\partial C}{\partial h} < 0, \quad \frac{\partial A}{\partial h} < 0 \quad \text{and} \quad \frac{\partial A}{\partial s} > 0 \tag{25}$$

so that

$$\frac{dC}{ds} < \frac{\partial C}{\partial s}\left(= \frac{C}{s}\right). \tag{26}$$

For finite amplitude changes ΔC and Δs, the quantity

$$\zeta = \frac{C}{s}\left(\frac{\Delta C}{\Delta s}\right)^{-1} \tag{27}$$

is termed the 'buffer', 'evasion' or 'Revelle' factor.

It can be determined graphically by plotting isolines of A and C in the s-h plane. Changes in the equilibrium state induced by changes in the carbon content lie along an alkalinity isoline. The intercepts with the C isolines determine the simultaneous values C, s and h that belong to any equilibrium state on the alkalinity curve. In practice, it is more convenient to plot A against $A-C$ (Fig. 26), as (through the dominance of $[HCO_3]$ in both expressions) the isolines of A and C are almost parallel.

More insight into the dynamics can be gained from an inspection of the differential buffer factor

$$\zeta' = \frac{C}{s}\left(\frac{dC}{ds}\right)^{-1}. \tag{28}$$

The expression for dC/ds contains a difference in two terms of the same order of magnitude. A regrouping of terms yields a more transparent form which contains only positive terms,

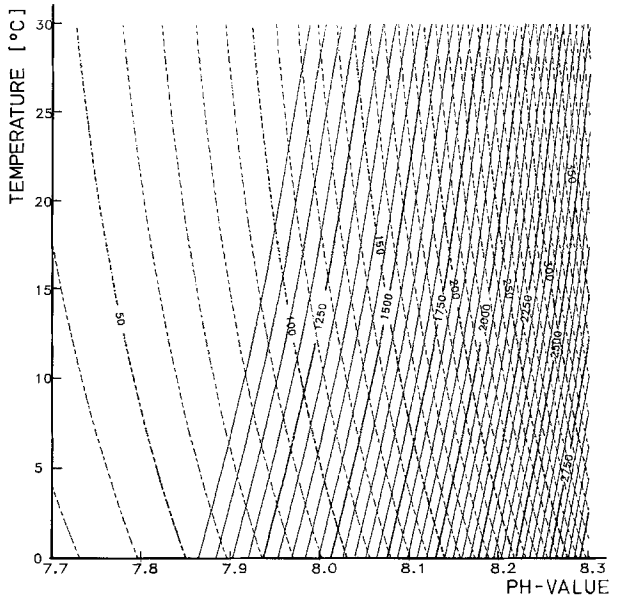

Fig. 26. Alkalinity and difference ΣCO_2-alkalinity as function of pCO_2 and pH-value

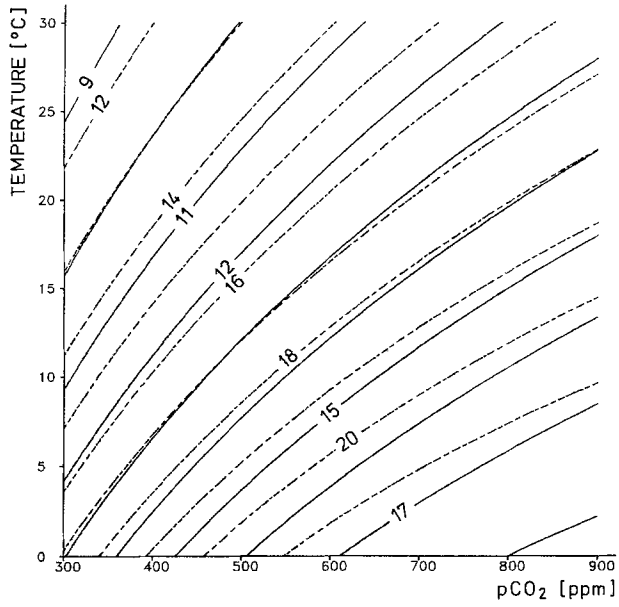

Fig. 27. Differential buffer factor as a function of temperature and pCO_2 *(solid lines)*. *Dashed lines* show the buffer factor which would result by neglecting the buffer capacity of the borate system

$$\frac{dC}{ds} = \frac{4\frac{K_1K_2}{h^2} + \frac{K_1}{h} + \frac{K_1^2K_2}{h^3} + \frac{h}{s}\left(1 + \frac{K_1K_2}{h^2} + \frac{K_1}{h}\right)\left[\frac{K_w}{h^2} + 1 + \frac{B_t}{K_B}\frac{1}{(1+h/K_B)^2}\right]}{4\frac{K_1K_2}{h^2} + \frac{K_1}{h} + \frac{h}{s}\left[\frac{K_w}{h^2} + 1 + \frac{B_t}{K_B}\frac{1}{(1+h/K_B)^2}\right]}. \tag{29}$$

The role of the borate system is seen from an inspection of the derivative with respect to B_t.

$$\Delta\zeta'_{B_t} = B_t \frac{d}{dB_t} \frac{dC}{ds}. \tag{30}$$

Insertion of realistic numbers into Eqs. (29) and (30) indicates that the borate system increases the ocean CO_2 storage capacity by more than 20%. Figure 27 shows the buffer factor (28) as a function of pCO_2 and temperature, using the full chemistry (solid lines) and neglecting the borate term in the term $\partial A/\partial h$ (broken lines) assuming an alkalinity of 2420 μeq/kg and a mean salinity of 35‰.